Microscopic examination of rf-cavity-quality niobium films through local nonlinear microwave response

Chung-Yang Wang,[1,*] Carlota Pereira,[2] Stewart Leith,[2] Guillaume Rosaz,[2]
and Steven M. Anlage[1]

[1]*Department of Physics, Quantum Materials Center, University of Maryland, College Park, Maryland 20742, USA*
[2]*CERN, European Organization for Nuclear Research, Geneva 23 1211, Switzerland*

The performance of superconducting radio-frequency (SRF) cavities is sometimes limited by local defects. To investigate the rf properties of these local defects, especially those that nucleate rf magnetic vortices, a near-field magnetic microwave microscope is employed. Local third-harmonic response (P_{3f}) and its temperature dependence and rf power dependence are measured for one Nb/Cu film grown by direct current magnetron sputtering (DCMS) and six Nb/Cu films grown by high-power impulse magnetron sputtering (HiPIMS) with systematic variation of deposition conditions. Five out of the six HiPIMS Nb/Cu films show a strong third-harmonic response that is likely coming from rf vortex nucleation due to a low-T_c surface defect with a transition temperature between 6.3 and 6.8 K, suggesting that this defect is a generic feature of air-exposed HiPIMS Nb/Cu films. A phenomenological model of surface-defect grain boundaries hosting a low-T_c impurity phase is introduced and studied with time-dependent Ginzburg-Landau (TDGL) simulations of probe-sample interaction to better understand the measured third-harmonic response. The simulation results show that the third-harmonic response of rf vortex nucleation caused by surface defects exhibits the same general features as the data, including peaks in third-harmonic response with temperature, and their shift and broadening with higher microwave amplitude. We find that the parameters of the phenomenological model (the density of surface defects that nucleate rf vortices and the depth an rf vortex travels through these surface defects) vary systematically with film deposition conditions. From the point of view of these two properties, the Nb/Cu film that is most effective at reducing the nucleation of rf vortices associated with surface defects can be identified.

I. INTRODUCTION

In high-energy physics, there is continued interest in building next-generation particle accelerators (for example, the International Linear Collider, ILC) using bulk Nb superconducting radio-frequency (SRF) cavities [1,2]. For the ILC, around 10 000 SRF cavities will be built.

The quality of an SRF cavity is typically quantified by its quality factor (Q factor) as a function of the accelerating gradient for the particle beam. Real-world materials are not perfect. The Q factors of SRF cavities are usually below their theoretical predictions. In particular, as the accelerating gradient, and hence the rf magnetic field on the Nb surfaces, becomes strong, the Q factor drops significantly (this is called the Q slope) [3–6]. Such a Q-slope phenomenon limits the rf field supported by the SRF cavities, which then limits the performance of the particle accelerator. Besides the Q-slope phenomenon, quenches are also frequently observed in many SRF cavities [7–9]. One reason for a quench is that a superconductor is locally heated up to exceed its critical temperature and loses superconductivity. Both the Q slope and defect-nucleated quenches indicate that the performance of SRF cavities is limited by breakdown events below the theoretically predicted intrinsic critical field of the superconductor [1,4,5]. These breakdowns are sometimes caused by uncontrolled local defects [10–12]. Candidates of defects in SRF cavities include oxides [13–17], impurities [18,19], grain boundaries [20–26], dislocations [25,27,28], surface roughness [29,30], etc. To make high Q-factor SRF cavities that operate to high accelerating gradients, it is necessary to understand these defects, in particular, their influence on the rf properties of SRF cavities. Therefore, there is a need to understand in detail the rf properties of these local defects.

*Contact author: chyawang@terpmail.umd.edu

In SRF material science, various kinds of techniques have been developed to characterize SRF cavities and SRF materials. For example, researchers routinely measure the Q factor [31] and residual resistance [32] of SRF cavities. However, it is costly and time consuming to fabricate and measure an entire cavity. As a result, many measurements are performed on coupon samples of SRF materials, including measurements of rf quench field [9,33,34] and surface resistance [33–36].

Another quantity of interest is the vortex penetration field because SRF cavities are expected to operate best in the Meissner state (vortex-free) to avoid dissipation due to vortex motion [9,20,30,37,38]. Superconductors show strong nonlinearity in the presence of vortices and show relatively weak nonlinearity in the vortex-free Meissner state. The nonlinear electrodynamic response arises when properties of the superconductor (such as the superfluid density) become time-dependent during the rf cycle. One manifestation of nonlinearity is that the superconductor creates response currents to the stimulation at frequencies other than the driving frequency. Utilizing the connection between vortices and nonlinearity, the vortex penetration field can be determined by measuring the third-harmonic response of a superconductor subjected to a time-harmonic magnetic field [39]. In particular, the vortex penetration field of thin films and multilayer structures have been studied with such ac (kHz regime) third-harmonic response magnetometry [38,40–46].

The techniques described above (Q factor, residual resistance, rf quench field, surface resistance, vortex penetration field, etc.) help physicists to characterize the global properties of SRF materials. However, none of them can directly study the local rf properties of SRF materials.

Motivated by the need to study rf properties of local defects, we successfully built and operated a near-field magnetic microwave microscope using a scanned loop (the original version) [47–51] as well as a magnetic writer from a magnetic recording hard-disk drive (the microwave microscope adopted in this work) [52–57] to measure locally generated third-harmonic response. The spatial resolution of the local probe of the microwave microscope is in the submicron scale, and the excitation frequency is in the range of several GHz.

Our microwave microscope offers a complementary view of the material properties that limit SRF cavity performance. The quantities of interest in a finished SRF accelerator cavity are the quality factor Q, the surface resistance of the material making up the walls of the cavity, and the changes in Q as the accelerating gradient of the cavity is increased. It is desirable to maintain a high Q factor up to the point where the superconductor reaches its critical surface magnetic field. Our microscope measures local electrodynamic properties of small samples of materials that make up SRF cavities. It utilizes nonlinear response that results from strong and inhomogeneously imposed rf magnetic fields as a surrogate for the high-gradient conditions experienced by the materials inside an SRF cavity. The microscope applies surface magnetic fields quite different from those in an SRF cavity, and imposes unique electromagnetic stresses to the material under study. Note that the Ohmic losses of superconducting materials in the microwave range at temperatures substantially below T_c are well below the sensitivity limit of any existing microwave microscope, hence these properties are not studied.

Bulk Nb is the standard choice for fabricating SRF cavities. The main reason is that Nb has the highest critical temperature ($T_c = 9.3$ K) and the highest first critical field ($B_{c1} = 180$ mT) of all the elemental metals at ambient pressure. Besides bulk Nb, there are some candidate alternative materials for SRF applications [58], including Nb film on Cu [18,30,35,37,59–63], Nb_3Sn on bulk Nb substrate [9,20,26,64–67], multilayer structure (superconductor-insulator-superconductor structures, for instance) [6,29,38,40,68–70], etc. The potential benefits of using materials other than bulk Nb would be a higher T_c and a potentially higher critical field B_c. Here we focus on Nb films on Cu.

The development of the deposition of Nb films onto Cu cavities has a long history [71]. In particular, the first Nb/Cu cavities were produced at CERN in the early 1980s [72]. Motivations for Nb thin-film technology for SRF applications include reducing material cost (high-purity Nb costs around 40 times more than Cu) and better thermal stability. In particular, at frequencies around 300 to 400 MHz, Nb/Cu cavities allow operation at 4 K instead of 2 K, due to the superior thermal conductivity of Cu. The performance of bulk Nb cavities is approaching the intrinsic limit of the material. In contrast, Nb/Cu cavities typically suffer from serious Q-slope problems [73,74], which limits their use in high accelerating fields. Solving the Q-slope problem in Nb/Cu cavities is essential for making them competitive for use in high-field accelerators.

In this work, we use our near-field magnetic microwave microscope to study the local third-harmonic response (on submicron scales, at several GHz) of SRF-quality Nb/Cu films produced at CERN. Our objective is not to provide a comprehensive characterization of all types of surface defects present in these Nb/Cu films. Surface defects that do not nucleate rf vortices fall outside the scope of this study. Instead, our focus is on locally measuring the third harmonic response to explore the surface defects that do nucleate rf vortices. Specifically, we aim to extract the properties of rf vortices linked to surface defects through experiments and simulations investigating the third-harmonic response and its dependence on temperature and rf field amplitude. Subsequently, we conduct a qualitative comparison of these Nb/Cu films based on our findings. This allows us to identify the Nb/Cu film that

is most effective at reducing the nucleation of rf vortices associated with surface defects.

The outline of this paper is as follows: In Sec. II, we describe the experimental setup. In Sec. III, we show the experimental results of these Nb/Cu films and focus on surface defect signals. In Sec. IV, we perform time-dependent Ginzburg-Landau (TDGL) simulations to better understand the experimental results. Through these simulations, we compare the Nb/Cu films and determine which film is most effective at reducing the nucleation of rf vortices associated with surface defects. In Sec. V, we summarize the results on the Nb/Cu films.

II. EXPERIMENTAL SETUP

The setup of our near-field magnetic microwave microscope (identical to that described in Ref. [57]) is described in this section. A schematic of the setup is shown in Fig. 1.

The heart of our microwave microscope is the magnetic writer head (provided by Seagate Technology) that is used in conventional hard-disk drives. The central part of the magnetic writer head is basically a solenoid that generates a localized rf magnetic field. The solenoid is in the submicron scale, which sets the spatial resolution of our microscope. In the setup, a Seagate magnetic writer head is attached to a cryogenic XYZ positioner (submicron spatial resolution) and used in a scanning probe microscope fashion. The probe is in contact with the sample during the third-harmonic measurement. However, the surfaces of the probe and sample are not perfectly flat, resulting in a finite probe-sample separation h, which influences the spatial resolution of the microscope and the peak microwave magnetic field experienced by the sample B_{pk}. The height h is estimated to be less than 1 micron, and the spatial resolution is estimated to be in the submicron scale, and B_{pk}

is estimated to fall within the range of tens of mT for a 0-dBm input microwave power [57].

The microwave source signal $P_{rf} \sin^2(\omega t)$ is sent to the probe (magnetic writer head) by its built-in and highly engineered transmission line. The probe then produces a local (submicron scale) rf magnetic field $B_{rf} \sin(\omega t)$ acting on the sample surface. The superconducting sample then generates a screening current on the surface in an effort to maintain the Meissner state. This screening current generates a response magnetic field that is coupled back to the same probe, creating a propagating signal whose third-harmonic component $P_{3f} \sin^2(3\omega t)$ is measured by a spectrum analyzer at room temperature. The third-harmonic response P_{3f} is measured because it arises from both the nonlinear Meissner effect [75,76], and when a vortex penetrates the sample surface and forms a vortex semiloop [77] (as discussed in Sec. I), either due to an intrinsic mechanism or local defects (weak spot for a vortex to penetrate).

Measurements of superconductor nonlinear response show tremendous dynamic range, often more than 20 dB [52,53,55–57]. The excellent instrumental nonlinear background of our measurements (approximately −155 dBm) allows for very sensitive measurements of superconductor nonlinearity and its variation with temperature, driving rf power, location, and probe-sample separation. Note that measurements are recorded in dBm and later converted to linear power for further study.

To improve the signal-to-noise ratio, microwave filters are installed as follows. Low-pass filters are installed between the microwave source and the probe to block the unwanted harmonic signals generated by the microwave source. High-pass filters are installed between the probe and the spectrum analyzer to block the fundamental input frequency signal from reaching the spectrum analyzer and producing unwanted nonlinear signals.

Measurements are performed with a variety of fixed-input frequencies between 1.1 and 2.2 GHz, while varying temperature and applied rf field amplitude. No external dc magnetic field is applied. The measured residual dc field near the sample at low temperatures is around 35 μT, as measured by a cryogenic three-axis magnetometer.

The base temperature for a sample in the cryostat is around 3.5 K. The sample and the thermometer are both directly mounted on the cold plate of the cryogen-free refrigerator to ensure good thermalization.
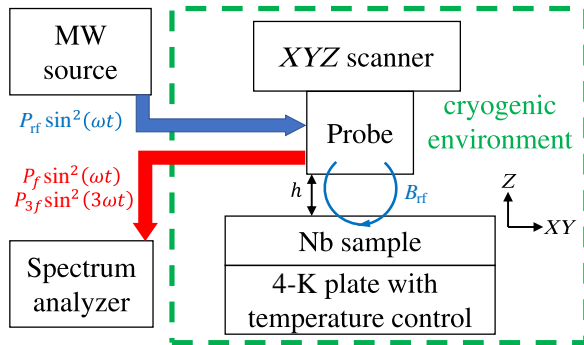

FIG. 1. Schematic of experiment setup. The microwave source (MW source) sends a signal of $P_{rf} \sin^2(\omega t)$ to the magnetic writer (Probe), which then generates $B_{rf} \sin(\omega t)$ acting on the sample surface locally. The sample response is collected by the same magnetic writer, and the third Fourier component $P_{3f} \sin^2(3\omega t)$ is studied. The dashed line box represents the cryostat.

III. EXPERIMENTAL RESULTS

In this work, we study seven Nb films deposited on one common Cu substrate, as shown in Fig. 2. One of the samples is prepared by direct current magnetron sputtering (DCMS) with zero bias, and the sample thickness is around 3.5 μm. The other six samples are prepared by high-power impulse magnetron sputtering (HiPIMS), with bias from
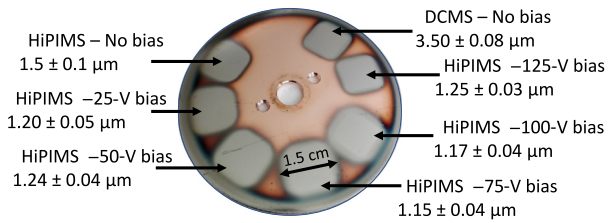
FIG. 2. Photo of the seven Nb films on one common Cu substrate. The samples are prepared at CERN.

0 to 125 V, and the sample thickness ranges from 1.15 to 1.5 μm. The preparation of the seven Nb/Cu films is discussed in Appendix A.

Our previous research investigated the third-harmonic response of both bulk Nb and Nb/Cu films [57]. However, maintaining a consistent probe-sample separation proved challenging due to the nonflat surfaces of the samples, which provided motivation for the samples created for the present work. In contrast, the Nb/Cu films examined in this study exhibit remarkable flatness, ensuring consistent probe-sample separation. Furthermore, HiPIMS Nb/Cu cavities fabricated at CERN show high repeatability [78], and the HiPIMS Nb/Cu films examined in this study adopt the same fabrication recipe. These two features enable us to conduct more meaningful comparisons between these samples.

In the following, the HiPIMS 25-V bias Nb/Cu sample is discussed in detail, and the results of all the seven Nb/Cu samples are summarized and compared in Table II and in Table III.

Figure 3 shows the representative data for the third-harmonic response power P_{3f} as a function of temperature at a fixed location on the HiPIMS 25-V bias Nb/Cu sample. A representative measurement protocol is as follows. The sample is warmed up to 10 K (above T_c), and then the microwave source is turned on with fixed-input frequency ($\omega/2\pi = 1.86$ GHz) and input power ($P_{rf} = +2$ dBm), and then P_{3f} is measured as the sample is gradually

cooled down to 3.5 K. In other words, the surface of the sample experiences a fixed rf field $B_{rf}\sin(\omega t)$ in a submicron scale area during the cooldown process from 10 to 3.5 K.

The measured $P_{3f}(T)$ in Fig. 3 can be decomposed into three segments: the region above 9.1 K, the region below 6.7 K, and the region in between. The magnetic writer head (the probe of our microwave microscope) itself has temperature-independent nonlinearity. The signal above 9.1 K comes from this probe background and is indeed temperature independent. A transition around 9.1 K can be seen in the inset of Fig. 3. This transition comes from the intrinsic nonlinear response of the Nb film. The strongest P_{3f} signal here shows up below 6.7 K. In the following, such a P_{3f} onset temperature is called the P_{3f} transition temperature and is denoted as $T_c^{P_{3f}}$. Compared to the signal around 9.1 K, the onset around 6.7 K is dramatic. Such a signal suggests that some mechanism shows up at and below 6.7 K that produces strong nonlinearity. The mechanisms leading to strong P_{3f} below 6.7 K are extrinsic and are likely due to surface defects. Note that P_{3f} below 6.7 K is much stronger than the intrinsic Nb signal around 9.1 K, suggesting that our local P_{3f} measurement is sensitive to surface defects.

Since the main objective of this work is investigating rf properties of surface defects, the strong P_{3f} below 6.7 K is the main focus in the following.

To further study the nature of P_{3f} below 6.7 K, $P_{3f}(T)$ for various input powers P_{rf} (and hence various applied rf field amplitudes B_{rf}) are measured. For each measurement, the sample is warmed up to 10 K and then cooled down to 3.5 K while experiencing an applied rf field with fixed-input frequency and input power. Since the measured P_{3f} is the combination of probe background and sample contribution, the probe background (probe background is obtained by averaging the magnitude of $P_{3f}(T)$ between 9.5 and 10 K) is subtracted from the total signal to isolate the sample signal. The process is repeated 6 times, each time with a different input power. The results of the six $P_{3f}(T)$ of different input powers (rf field amplitudes) are shown in the linear format in Fig. 4.

In Fig. 4, all the six $P_{3f}(T)$ exhibit a two-peak feature, and their $T_c^{P_{3f}}$ are consistently around 6.7 K. For both peaks, as the rf field amplitude increases (purple to red in Fig. 4), the $P_{3f}(T)$ maximum increases; in addition, the $P_{3f}(T)$ maximum and the $P_{3f}(T)$ low-temperature onset both show up at a lower temperature. These features of $P_{3f}(T)$ are listed in Table I. We will see that the four features of $P_{3f}(T)$ listed in Table I are the key features of all the nonlinear data in the sense that they show up in all the Nb/Cu films measurement results (see Figs. 4 and 6) and also in numerical simulations of superconductor nonlinear response (see Figs. 9, 13, and 14).

So far the measurements are taken at one single location on the surface of the sample. How about the situation at
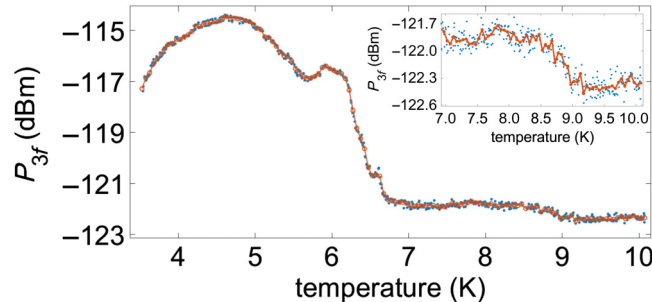

FIG. 3. Representative data for P_{3f} as a function of temperature for the HiPIMS 25-V bias Nb/Cu sample. The input frequency is 1.86 GHz and the input power is 2 dBm. The blue dots are the raw data, and the red curve is the P_{3f} averaged over 0.05-K range bins. Inset: enlargement of the figure above 7 K.
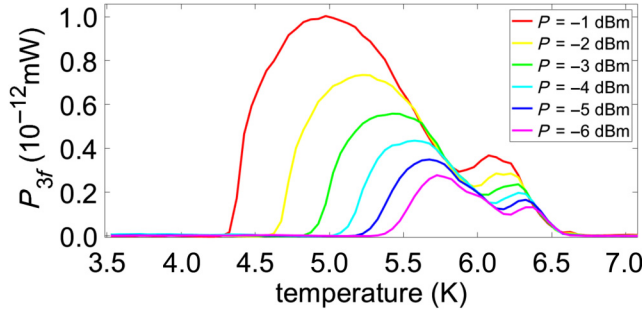
FIG. 4. Measured linear power scale $P_{3f}(T)$ from strong (red) to weak (purple) input power for the HiPIMS 25-V bias Nb/Cu sample. The input frequency is 1.86 GHz. Compared to the raw data shown in Fig. 3, here the probe background is subtracted. Note that input power (in dBm scale) is proportional to B_{rf}^2, and hence $B_{rf}^{red} = 1.78 B_{rf}^{purple}$.
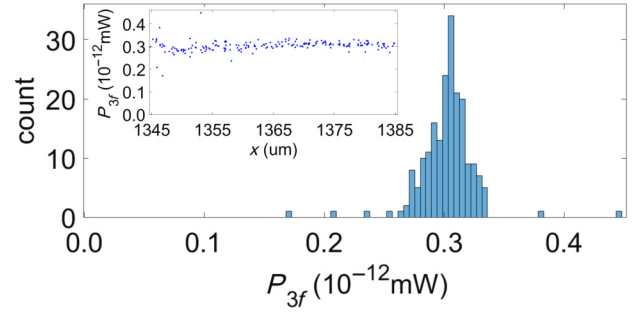

FIG. 5. Statistics of one-dimensional scan for $P_{3f}(T = 5.7$ K, $P = -5$ dBm, $f = 1.86$ GHz) for the HiPIMS 25-V bias Nb/Cu sample. The coefficient of variation (the ratio of the standard deviation to the mean) is 0.08. Inset: spatial distribution of this one-dimensional scan.

other locations? In particular, does the defect signal (the strong P_{3f} below 6.7 K) show up at other locations as well? To answer this question, we measure $P_{3f}(T)$ with $P = -2$ dBm at four distinct locations on the sample surface and obtain consistent results. The separation between any two of these locations exceeds 10 μm. In addition, a one-dimensional (1D) scan is performed for a 40-μm range with a step size of 0.2 μm. Temperature and input power are chosen to be $T = 5.7$ K and $P = -5$ dBm, and our goal is to determine the homogeneity of the signal from the lower-temperature peak of the blue curve in Fig. 4. The 1D scan result is shown in Fig. 5. According to this scanning result, the P_{3f} signal from the defect is quite consistent and uniform at the μm scale (coefficient of variation = 0.08). One possible explanation of such uniformity is that the size of one single defect is at the nm-scale and the defect spacing is smaller than the resolution of the microscope (submicron scale), and hence the P_{3f} signal of our submicron scale measurements comes from the contributions of multiple defects. As an example, the average grain size is around 390 nm for the HiPIMS Nb/Cu films studied in Ref. [35] (p. 3 of Ref. [35]). Suppose the HiPIMS Nb/Cu films studied in this work have a similar structure to those in Ref. [35], and suppose the surface defects

responsible for the P_{3f} signal in Fig. 5 are grain boundaries. In that case, a microwave microscope with a resolution significantly better than 400 nm is required to resolve P_{3f} signals from two distinct grain boundaries.

So far only the HiPIMS 25-V bias Nb/Cu sample has been discussed. Temperature dependence and input-power dependence of P_{3f} are studied for the other six Nb/Cu samples in the same manner as the HiPIMS 25-V bias Nb/Cu sample. The HiPIMS 25-V bias Nb/Cu sample $P_{3f}(T)$ shows the two-peak feature, suggesting that the measured $P_{3f}(T)$ is the superposition of two defect signals. On the other hand, for some of the Nb/Cu samples (75-V bias, 100-V bias, 125-V bias), the $P_{3f}(T)$ defect signal shows a single-peak structure, suggesting that the measured $P_{3f}(T)$ captures only one defect signal. Figure 6 shows the representative $P_{3f}(T)$ for the 75-V bias sample [Fig. 6(a)] and the 125-V bias sample [Fig. 6(b)]. For both Figs. 6(a) and 6(b), $P_{3f}(T)$ displays Features 1, 2, and 3 (Table I), suggesting that these features are quite universal. Although we have no access to the temperature regime below 3.5 K, Feature 4 (Table I) is likely to be present based on $P_{3f}(T)$ above 3.5 K.

The results of the defect signal and the Nb signal of all seven Nb/Cu samples are summarized in Table II. For the six HiPIMS Nb/Cu samples, it is quite universal that P_{3f} measurements reveal the intrinsic Nb signal around 9 K and the extrinsic defect signal at low temperatures. Specifically, the defect signal with $T_c^{P_{3f}}$ between 6.3 and 6.8 K is observed for five out of the six HiPIMS Nb/Cu samples, suggesting that such a defect is a generic feature for these HiPIMS Nb/Cu samples. Moreover, the defect signals are always much stronger than the intrinsic Nb signal around 9 K, like the situation shown in Fig. 3. Scanning measurements are performed for three HiPIMS samples (25-V bias sample, 50-V bias sample, and 125-V bias sample), and the results show that the defect signals are quite uniform at the μm scale for all three samples. Data for the HiPIMS 50-V bias sample, the HiPIMS 100-V bias sample and

TABLE I. The four key features of $P_{3f}(T)$ in our measurements of Nb/Cu films.

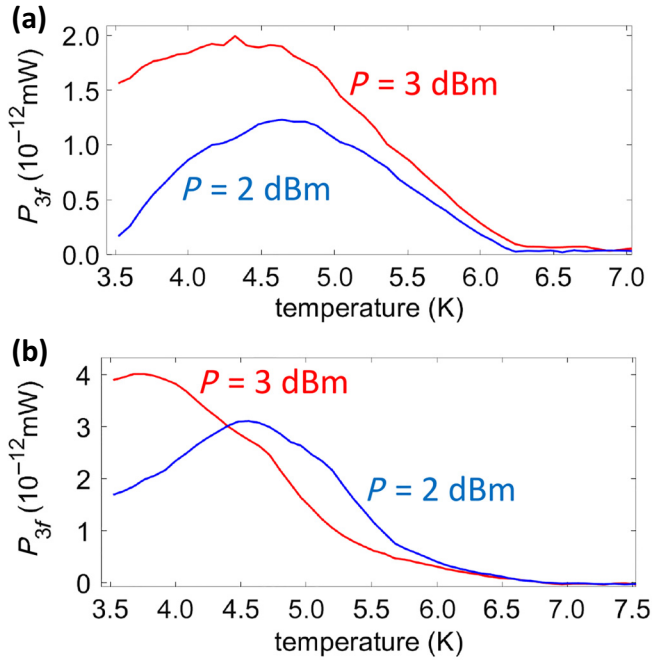|	
Feature 1	$P_{3f}(T)$ onsets below T_c of Nb and shows a bell-shaped structure.
Feature 2	$P_{3f}(T)$ maximum increases for a stronger rf field amplitude.
Feature 3	$P_{3f}(T)$ maximum shows up at a lower temperature for a stronger rf field amplitude.
Feature 4	$P_{3f}(T)$ low-temperature onset shows up at a lower temperature for a stronger rf field amplitude.

(a)

(b)

FIG. 6.   Measured $P_{3f}(T)$ for two input powers for the HiPIMS 75-V bias Nb/Cu sample with an input frequency of 1.98 GHz (a) and for the HiPIMS 125-V bias Nb/Cu sample with an input frequency of 1.66 GHz (b).

the DCMS sample are shown in Appendix B. Data for the HiPIMS 0-V bias sample is qualitatively different from all the other six samples and is discussed in Appendix C. It is worth noting that the third-harmonic response of a Nb/Cu film in our previous research [57] also revealed surface defects, with T_c^{P3f} around 6.76 K (see Table I of Ref. [57]). See Appendix D for further discussion comparing our previous research [57] and this study.

In all the measurements discussed so far, $P_{3f}(T)$ is measured as a function of decreasing temperature starting

TABLE II.   Summary of the defect signal (red) and the Nb signal (blue) of the seven Nb/Cu samples. See Appendix C for the discussion of the HiPIMS 0-V bias sample.

Sample	Fixed-point measurement	Scanning
HiPIMS, 125-V bias	$T_c^{\mathrm{P3f}} = 6.8$ K defect	is everywhere
HiPIMS, 100-V bias	Nb signal around 8.8 K	N/A
	$T_c^{\mathrm{P3f}} = 6.5$ K defect	N/A
HiPIMS, 75-V bias	$T_c^{\mathrm{P3f}} = 6.3$ K defect	N/A
HiPIMS, 50-V bias	Nb signal around 8.9 K	
	$T_c^{\mathrm{P3f}} = 6.4$ K defect	is everywhere
	$T_c^{\mathrm{P3f}} = 6.8$ K defect	is everywhere
HiPIMS, 25-V bias	Nb signal around 9.1 K	
	two of $T_c^{\mathrm{P3f}} = 6.7$ K defects	are everywhere
HiPIMS, no bias	Nb signal around 9 K	N/A
	defect signal	N/A
DCMS, no bias	$T_c^{\mathrm{P3f}} = 6.5$ K defect	N/A

above T_c (from 10 to 3.5 K). One may wonder whether this procedure produces trapped vortices when a Nb film cools down through its T_c. To address this issue, we consider the effects of the two magnetic fields involved: the residual dc field and the applied rf field. The average flux quanta separation ($\sqrt{\Phi_0/B}$) corresponding to the residual dc field near the sample (around 35 μT) is around 7.7 μm, which is much larger than the spatial resolution of the microscope (submicron scale). Therefore, with high probability, there is no dc flux beneath the microscope probe, even if the 35 μT residual dc field is completely trapped. Regarding the rf field, the rf vortices are transient, appearing and disappearing twice per rf cycle. Compared to the dynamics of an rf vortex (on the order of nanoseconds), the temperature change during a typical cool down is in the extreme adiabatic limit. To the best of our knowledge, there is no unambiguous evidence suggesting that an rf vortex can be converted to a dc vortex and trapped as a Nb film cools down through T_c. One way to verify whether rf vortices are trapped in our setup is to compare $P_{3f}(T)$ taken in a warm-up process to $P_{3f}(T)$ taken in a cool-down process for a sample showing a defect signal (such a study is presented in Appendix E). As shown in Fig. 18, $P_{3f}(T)$ does not exhibit a clear hysteresis, which justifies our interpretation about the absence of trapped dc vortices as the Nb film cools down through T_c in the presence of an rf field.

IV. DISCUSSION

The objective of this section is to better understand the third-harmonic response associated with rf vortices nucleating at surface defects through numerical simulations, and then using these insights to analyze the experimental results further. In the following, we first introduce our simulation framework (Sec. IV A). As a warm up, we consider the case of a defect-free bulk Nb ($T_c = 9.3$ K) (Sec. IV B) for developing central concepts relevant to rf vortex nucleation and nonlinear response. Next, we propose a phenomenological surface defect toy model (Sec. IV C) whose P_{3f} shares common features with the experimental results (the four key features in Table I). Specifically, the temperature dependence and the rf field amplitude dependence of P_{3f} can be qualitatively explained by the two parameters ("how deep an rf vortex semiloop penetrates into a sample through a surface defect" and "the number of surface defects that nucleate rf vortices in each half of the rf cycle") of the toy model (Secs. IV D and IV E). Finally, we conduct a qualitative comparison of these Nb/Cu films based on these two parameters (Sec. IV F).

A. Introduction to numerical simulations

In our measurements, the applied field is a localized rf magnetic field instead of a uniform dc magnetic field. In addition, the configuration of the rf magnetic field

produced by the probe is nonuniform but is similar to the field produced by a point dipole. In other words, the situation is different from the case of "a constant dc magnetic field parallel to the sample surface." The probe also produces a more aggressive magnetic field than the one present in an SRF cavity. Instead of being nominally parallel to the surface, the rf magnetic field has a substantial normal component to the surface. As a result, it is required to study the third-harmonic response more carefully.

The time-dependent Ginzburg-Landau (TDGL) model is widely used for studying vortex behavior in superconductors [20,29,79–84]. In particular, vortices (see Sec. IV B) and the proximity effect (see Sec. IV C) are incorporated naturally in TDGL simulations and hence TDGL is a good tool for SRF material science. To better understand our data, numerical simulations of the TDGL equations are performed. The full TDGL equations must be solved in this case because the superconductor is subjected to a time-dependent and inhomogeneous rf magnetic field. We do not assume or impose any spatial symmetries in the model, and solve Maxwell's equations for the dipole in free space above the superconductor, as well as inside the superconductor [79]. The TDGL equations solved are the same as those discussed in Ref. [79]. The equations, boundary conditions and material parameters of the TDGL simulations can be found in Appendix F and in Table V.

In the simulations, the smooth and flat superconducting sample occupies the $z < 0$ region, and the magnetic writer probe is approximated to be a pointlike magnetic dipole with a sinusoidal time-dependent magnetic moment $(M_{dp} \sin(\omega t), 0, 0)$ (namely an rf magnetic dipole pointing in the x direction) whose frequency is $\omega/2\pi = 1.7$ GHz. The rf dipole is located at $(0, 0, h_{dp})$ with $h_{dp} = 400$ nm. That is, the rf magnetic dipole is above the superconducting sample and parallel to the surface of the sample. Since the magnetic field produced by the rf dipole is nonuniform, the peak rf magnetic field amplitude experienced by the superconductor is specified and is denoted as B_{pk}. Here $(x, y, z) = (0, 0, 0)$ is the location in the sample that experiences the strongest field, and hence B_{pk} is the rf field amplitude at $(x, y, z) = (0, 0, 0)$. Because the rf field is localized, nontrivial dynamics of the sample (vortex nucleation, for example) would show up only in the region that is underneath the rf magnetic dipole (namely near $(x, y, z) = (0, 0, 0)$), while the region that is far away from the rf magnetic dipole would be in the vortex-free Meissner state.

In the simulations, TDGL is used to calculate the time evolution of the order parameter and the vector potential as the superconducting sample is stimulated by the time-dependent rf field produced by the horizontal point dipole above it. (There is no dc magnetic field in the simulations.) With the order parameter and the vector potential, the screening current and hence the magnetic field associated with that screening current (response of the sample)

can be calculated. The response magnetic field is calculated at the location of the point dipole and it is assumed that this time-varying magnetic field induces a voltage wave that propagates up to the spectrum analyzer at room temperature. The quantity $\sqrt{P_{3f}}$ is proportional to the third-harmonic Fourier component of the magnetic field (generated by the screening current) at the dipole location.

Most TDGL treatments assume a two-dimensional sample and fields that are uniform in the third dimension. This oversimplifies the problem. It creates "artificial features that extend uniformly" in the third dimension and thus creates infinitely long vortices in the superconductor. Our approach (multidomain three-dimensional simulation) does not make such unrealistic assumptions. In addition, our experiment and model examine the properties of finite-sized magnetic vortex semiloops, which are thought to be the generic types of rf vortex excitations created at the surface of SRF cavities [77].

B. Calculated bulk Nb nonlinear response

Unlike a dc vortex whose behavior shows no time dependence, an rf vortex shows nontrivial dynamics, and should be examined in a time-domain manner. Here we demonstrate the time-domain analysis (focusing on the dynamics of rf vortices) for a specific rf field amplitude ($B_{pk} = 61.6$ mT) and a specific temperature (8.23 K). (Material parameters of Nb are used in the defect-free bulk Nb simulations. See Appendix F and Table V.)

The dynamics of rf vortex semiloops for bulk Nb during the first half of an rf cycle (frequency = 1.7 GHz, period = 5.88×10^{-10} s) is shown in Fig. 7, for a fixed rf field amplitude ($B_{pk} = 61.6$ mT) and a fixed temperature (8.23 K). Figures 7(a)–7(g) show the space and time dependence of the square of the normalized order parameter ($|\psi/\psi_\infty|^2$) (here 1 means full superconductivity and 0 means no superconductivity); the black region is where $|\psi/\psi_\infty|^2 < 0.03$. Since the order parameter is suppressed significantly at the center of a vortex core, a vortex can be visualized by tracking the black region. Here $\psi_\infty = \psi_\infty(T)$ is the value of the order parameter deep inside bulk Nb at temperature T.

In the early stage of the rf cycle, there is no rf vortex [Figs. 7(a) and 7(b)], and then an rf vortex semiloop that is parallel to the direction of the rf dipole (which points in the x direction) shows up [Figs. 7(c)–7(e) and 7(g)]. The rf vortex semiloop disappears later in the rf cycle [Fig. 7(f)]. Video 1 shows the nucleation, movement, and exit of the rf vortex semi-loop in bulk Nb in one rf cycle. The parameter setting can be found in the Supplemental Material [85].

Besides examining the spatial distribution of the order parameter, another signature of vortices is the phase of the order parameter. Because Ginzburg-Landau theory is based on the existence of a single-valued complex superconducting order parameter ($\psi = |\psi|e^{i\theta}$), the phase θ must

VIDEO 1. An animation showing the nucleation, movement, and exit of the rf vortex semiloop in bulk Nb in one rf cycle.
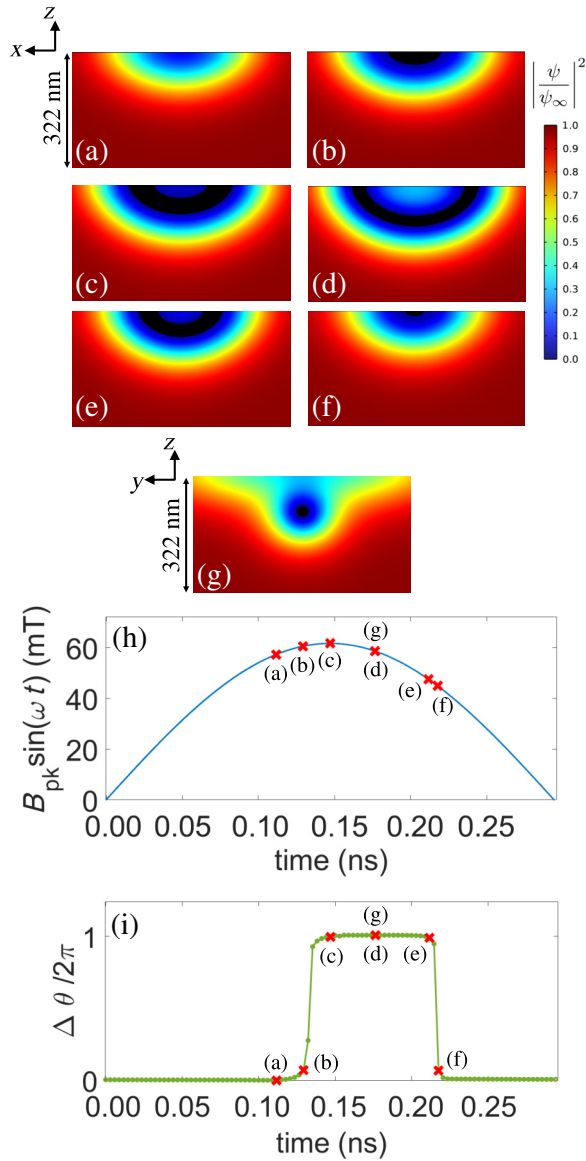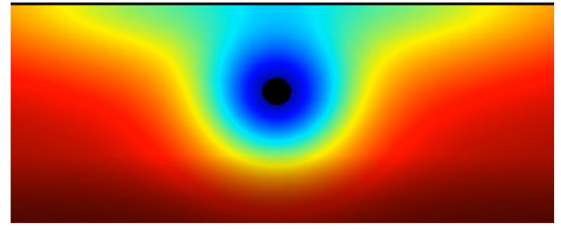
FIG. 7. Time-domain analysis for the dynamics of rf vortex semiloops in bulk Nb. A time-dependent magnetic moment (rf dipole) is 400 nm above the superconductor surface, pointing in the x direction, and producing $B_{pk} = 61.6$ mT at $T = 8.23$ K. (a)–(f) show the square of the normalized order parameter ($|\psi/\psi_\infty|^2$) on the X-Z plane cross section at different times during the first half of the rf period. The black region is where $|\psi/\psi_\infty|^2 < 0.03$. (g) shows $|\psi/\psi_\infty|^2$ on the Y-Z plane cross section at the same moment as (d). (h) rf field at $(x, y, z) = (0, 0, 0)$ versus time during the first half of the rf period. (i) Phase change for a closed contour (on the Y-Z plane) that is large enough to enclose the entire nontrivial region. Red crosses in (h) and (i) correspond to snapshots (a)–(g).

change by integral multiples of 2π in making a closed contour (see Eq. (4.45) in Ref. [86]), namely

$$\oint ds \cdot \nabla\theta = 2\pi N, \tag{1}$$

where N is a positive or negative integer, or zero. The integral $1/2\pi \oint ds \cdot \nabla\theta$ is quantized, and corresponds to the number of vortices enclosed by the closed contour.

Figure 7(i) shows the value of the integral $1/2\pi \oint ds \cdot \nabla\theta$ (namely $\Delta\theta/2\pi$) as a function of time. The contour is on the Y-Z plane and is large enough to enclose the entire nontrivial region. Note that Figs. 7(h) and 7(i) share a common horizontal axis. Based on Fig. 7(i), there are no vortices at the moments of (a), (b), and (f), and there is one vortex at the moments of (c), (d), and (e), which agrees with the order parameter analysis [Figs. 7(a)–7(g)].

The time-domain analysis described here [space and time dependence of the order parameter [Figs. 7(a)–7(g)] and $\Delta\theta/2\pi$ [Fig. 7(i)] is applied to all TDGL simulations whenever we check whether or not there are rf vortex semiloops.

Equipped with the picture of rf vortex nucleation, now let us move on to the resulting P_{3f}. The simulation result of $P_{3f}(T)$ for a fixed rf field amplitude ($B_{pk} = 61.6$ mT) for bulk Nb is shown in Fig. 8(a). The bell-shaped structure $P_{3f}(T)$ in Fig. 8(a) can be decomposed into three segments (separated by the two dashed vertical black lines) and can be understood with the vortex penetration field $B_{vortex}^{RF}(T)$ (see Fig. 9) and the strength of superconductivity. An rf vortex semiloop shows up when $B_{pk} > B_{vortex}^{rf}(T)$. Below 8.1 K, $B_{vortex}^{rf}(T) > B_{pk}$ and hence the entire bulk Nb is in the vortex-free Meissner state [see Fig. 8(b) and the purple curve in Fig. 8(f)], whose nonlinear response is weak. As temperature increases, $B_{vortex}^{rf}(T)$ decreases and hence B_{pk} would be greater than $B_{vortex}^{rf}(T)$ at a certain temperature depending on the strength of the rf stimulus. In this simulation ($B_{pk} = 61.6$ mT), from the full time-domain simulation (see the discussion for Fig. 7) one finds that there is one rf vortex semiloop (underneath the rf magnetic dipole) that penetrates the surface of the bulk Nb when the temperature is around 8.14 K [see Fig. 8(c) and the blue curve in Fig. 8(f)]. Roughly speaking, this implies that $B_{vortex}^{rf}(T = 8.14$ K$) \approx 61.6$ mT. As temperature increases, $B_{vortex}^{rf}(T)$ drops and vortex nucleation is favorable, and indeed the second rf vortex semiloop shows up around 8.6 K [see Fig. 8(e) and the red curve in Fig. 8(f)] and thus P_{3f} increases with temperature between 8.1 K and 8.8 K. Besides examining the order parameter [Figs. 8(b)–8(e)],
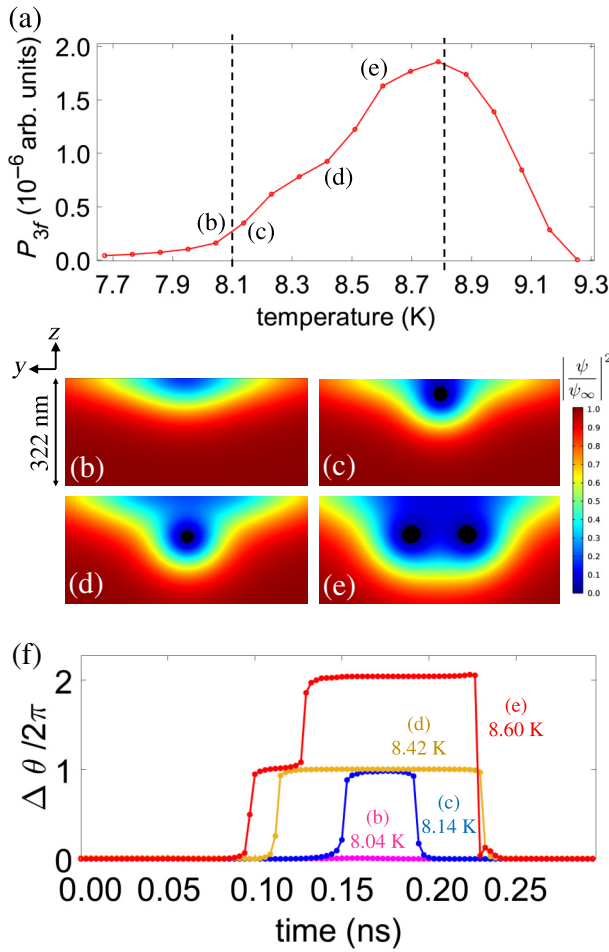
FIG. 8. (a) TDGL simulation result of $P_{3f}(T)$ for a fixed rf field amplitude ($B_{pk} = 61.6$ mT) imposed by a point dipole source for bulk Nb. From left to right, P_{3f} is weak at low temperatures (below 8.1 K), then increases with temperature (between 8.1 and 8.8 K), and drops with the temperature at high temperatures (above 8.8 K). (b)–(e) show $|\psi/\psi_\infty|^2$ on the Y-Z plane cross section at 8.04, 8.14, 8.42, and 8.60 K, respectively. The black region is where $|\psi/\psi_\infty|^2 < 0.03$. These snapshots are taken at $\omega t = 0.6\pi$. (f) shows $\Delta\theta/2\pi$ versus time for the four temperatures.

Fig. 8(f) also shows how the vortex number and duration change with temperature.

The nonlinear response of the superconductor is determined not only by the number of vortices (as described above in the language of $B_{vortex}^{rf}(T)$) but also by the strength of superconductivity. As the temperature approaches the transition temperature of a superconductor, its superconductivity and hence nonlinear response becomes weak. Such a temperature dependence leads to the decreasing tail of $P_{3f}(T)$ above 8.8 K in Fig. 8(a).

Figure 9(a) summarizes the simulation results of $P_{3f}(T)$ for three different rf field amplitudes for bulk Nb. For all three rf field amplitudes, P_{3f} is weak at low temperatures ($B_{pk} < B_{vortex}^{RF}(T)$, vortex-free Meissner state), arises at
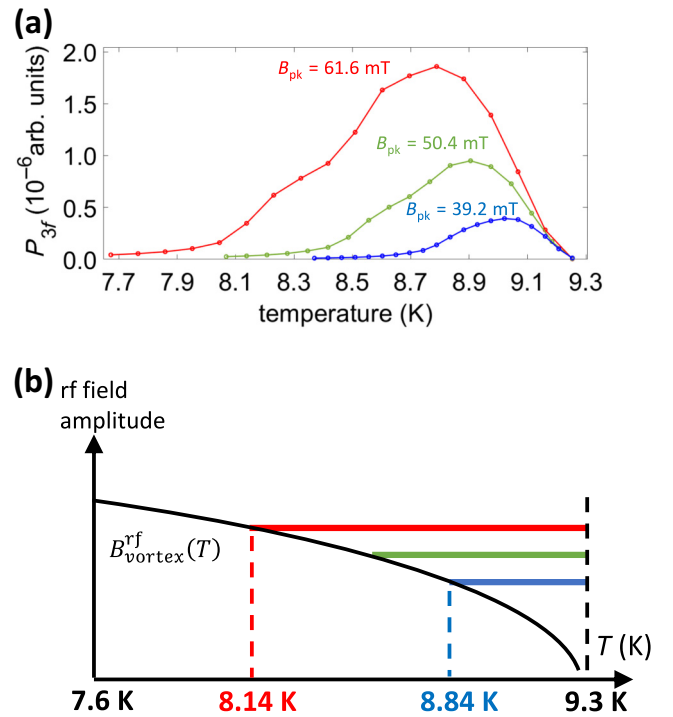

FIG. 9. (a) TDGL simulation result of $P_{3f}(T)$ for three different rf field amplitudes for bulk Nb. (b) Schematic of the vortex penetration field $B_{vortex}^{RF}(T)$ (the black curve) and the temperature range of $P_{3f}(T)$ bell-shaped structure for the three rf field amplitudes (the three colorful horizontal lines). The y axis is the rf field amplitude. Note that (a),(b) share the same horizontal axis and the same color-coded rf field amplitudes.

high temperatures ($B_{pk} > B_{vortex}^{RF}(T)$, rf vortex semiloops), and then drops with temperature as the temperature is near the critical temperature. For the red curve, the first vortex semiloop shows up around 8.14 K, which implies $B_{vortex}^{rf}(T = 8.14$ K$) \approx 61.6$ mT; for the blue curve, the first vortex semiloop shows up around 8.84 K, which implies $B_{vortex}^{rf}(T = 8.84$ K$) \approx 39.2$ mT. Figure 9(b) illustrates $B_{vortex}^{rf}(T)$ and the rf field amplitude dependence of the temperature range of $P_{3f}(T)$ bell-shaped structure. In this rf field amplitude-temperature phase diagram, the vortex-free Meissner state occupies the region below $B_{vortex}^{rf}(T)$ and rf vortex semiloops show up in the region above $B_{vortex}^{rf}(T)$. It is clear that the $P_{3f}(T)$ bell-shaped structure extends to lower temperatures as the rf field amplitude becomes stronger [from the blue to the green to the red in Figs. 9(a) and 9(b)] because of the temperature dependence of $B_{vortex}^{rf}(T)$, and this explains Feature 4 in Table I. Note that the four key features of $P_{3f}(T)$ (Table I) are clearly observed in Fig. 9(a) (except that the onset temperature of $P_{3f}(T)$ is equal to but not below 9.3 K since this simulation is for a defect-free bulk Nb), suggesting that these key features are signatures of rf vortex nucleation.

Equipped with the intuition of P_{3f} and rf vortex semiloops and their temperature dependence and rf field

amplitude dependence for the defect-free bulk Nb, now let us move on to the case with surface defects, which is the main focus of this paper.

C. Simulation of vortex nucleation in grain boundaries

Quantitatively comparing the details of the measured P_{3f} among different Nb/Cu films is challenging for two main reasons. Firstly, the specifics of P_{3f} depend on the probe-sample separation, which is difficult to reproduce. Secondly, different Nb/Cu films studied in this work might possess different types of surface defects that nucleate rf vortices. For example, grain boundaries may be the primary sources of P_{3f} for one Nb/Cu film, while dislocations could be the main sources of P_{3f} for another Nb/Cu film.

Although the details of rf vortex nucleation (and the resulting P_{3f}) by various surface defects are complicated and depend on details, we can analyze the dynamics of rf vortex nucleation in a phenomenological way and extract qualitative information. On the phenomenological level, the dynamics of rf vortices penetrating a sample surface through surface defects can be quantified by means of two key aspects: how many surface defects that nucleate rf vortices (ρ^{defect}) exist, and how deep do rf vortices travel into a sample through surface defects in half an rf cycle ($h_{\text{penetration}}^{\text{defect}}$)?

Here we illustrate the concept of $h_{\text{penetration}}^{\text{defect}}$ by considering rf vortex nucleation at grain boundaries in Nb films. For a given grain boundary that nucleates an rf vortex, the depth of the rf vortex travels into the Nb film through the grain boundary in half an rf cycle ($h_{\text{penetration}}^{\text{defect}}$) is determined by multiple factors, including the width of the grain boundary, the angle between the grain boundary and the Nb film surface, the material properties of the impurity phases in the grain boundary, etc. Instead of considering the details of all possible microstructures, we adopt a phenomenological approach, where $h_{\text{penetration}}^{\text{defect}}$ serves as the phenomenological characterization of the depth the rf vortex travels into the Nb film through the grain boundary in half an rf cycle.

Nb is known to contain low-T_c impurity phases, such as the oxides of Nb [13–17,87]. In such phases, oxygen forms a solid solution in Nb and produces materials with critical temperatures below the bulk T_c of pure Nb (9.3 K) [12,88,89]. Nb samples with higher oxygen content tend to have a lower critical temperature. For instance, T_c drops to around 7.33 K for 2% oxygen content, and drops to around 6.13 K for 3.5% oxygen content [89]. Another class of low-T_c impurity phases in Nb are the niobium hydrides [25,90], and some of these phases exhibit superconducting transitions around 1.3 K [91].

Motivated by the existence of these low-T_c impurity phases, here we consider a phenomenological surface-defect toy model in which the grain boundaries of Nb host the low-T_c material (impurity phases). Such grain boundaries might serve as weak spots for vortex nucleation. As shown later in this section, the proximity effect is active in this model of the grain boundaries. Here we consider one possible toy model realization of "Nb grain boundaries filled with low-T_c material." Of course, the phenomenological toy model (a grain-boundary model) considered here is just one possible scenario of surface defects that might be able to qualitatively explain the experimental results. rf vortices are more prone to nucleate at wide grain boundaries compared to narrow ones. Consequently, instead of characterizing a typical grain boundary in Nb/Cu films, the toy model is designed to characterize specifically those that are wide.

Figure 10 shows the side view of the grain-boundary model. By the very definition of $h_{\text{penetration}}^{\text{defect}}$, we constrain the rf vortices to only probe the region of $0 > z > -h_{\text{penetration}}^{\text{defect}}$, and hence the details in the region of $z < -h_{\text{penetration}}^{\text{defect}}$ play a minor role. As a result, this region can be treated as bulk Nb as an approximation. (In summary, $z = 0$, sample surface; $0 > z > -h_{\text{penetration}}^{\text{defect}}$, defect whose XY cross section is shown in Fig. 11(b); $z < -h_{\text{penetration}}^{\text{defect}}$, bulk Nb.) Here $h_{\text{penetration}}^{\text{defect}}$ is set to be 200 nm.

The rf dipole is located at $(0, 0, h_{\text{dp}})$ and hence vortex semiloops first show up near $(x, y, z) = (0, 0, 0)$. Therefore, the physics around the origin plays a dominant role. As an approximation, surface defects (Nb grain boundaries filled with low-T_c material) are introduced near the origin (illustrated in Fig. 10), while the region far away from the origin is set to be defect-free bulk Nb to reduce computational time. As a result, only the region around
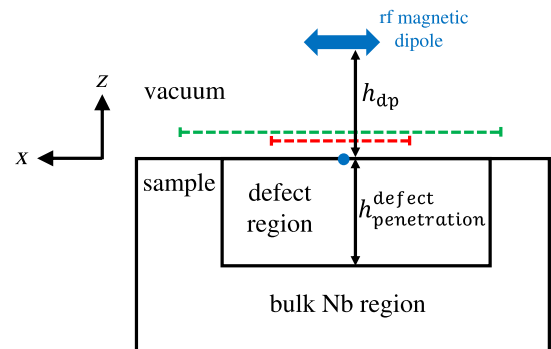

FIG. 10. Sketch of the side view (X-Z plane) of the grain-boundary model. The origin is marked by a blue dot. The rf dipole is represented by the blue arrow. The schematic is not to scale ($h_{\text{dp}} = 400$ nm and $h_{\text{penetration}}^{\text{defect}} = 200$ nm). Since the physics around the origin plays a dominant role, the region far away from the origin is set to be defect-free bulk Nb to reduce computational time. In addition, the region below $z = -h_{\text{penetration}}^{\text{defect}}$ is also set to be bulk Nb for simplicity. Note that the model is not cylindrically symmetric. The top view of the region indicated by the red dashed line is shown in Fig. 11(b), and the top view of the region indicated by the green-dashed line is shown in Fig. 19.
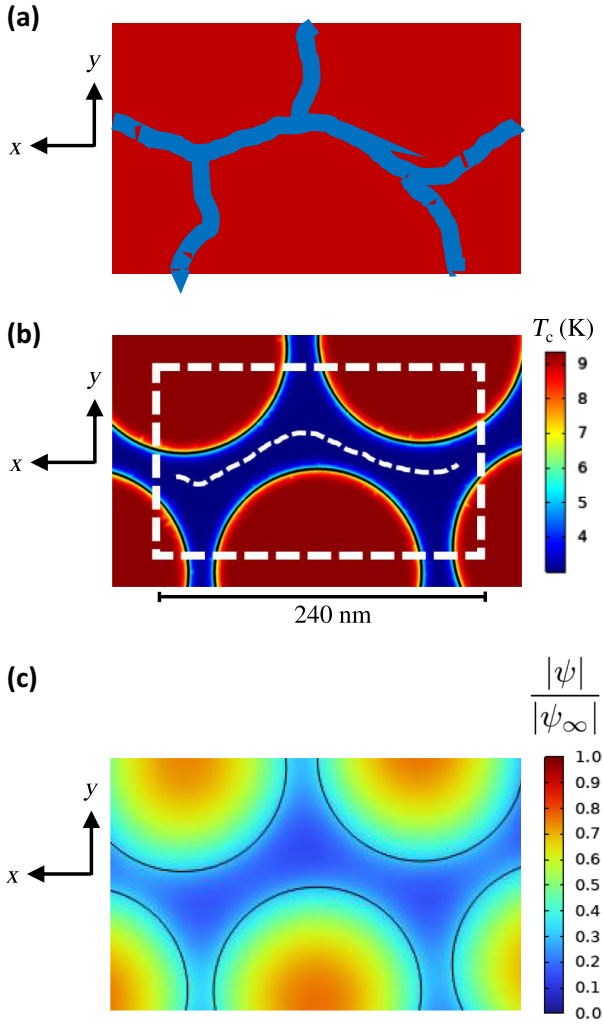
FIG. 11. A top view schematic of the grain-boundary model. (a) Illustration of Nb grains and grain boundaries, with red being Nb grains and blue being grain boundaries filled with impurity phases. The realization of this illustration used in the TDGL simulations is shown in (b). (b) The distribution of critical temperature on the X-Y plane around the origin (corresponds to the region indicated by the red dashed line in Fig. 10), with red being Nb and blue being the low-T_c impurity phase with $T_c^{impurity} = 3$ K. Here $(x, y, z) = (0, 0, 0)$ is at the center. The rf dipole is located at $(x, y, z) = (0, 0, 400$ nm) and points in the x direction. The white dashed curve indicates the grain boundary that is roughly parallel to the x direction. The model defect region is indicated by the white-dashed rectangle. (c) A snapshot of the distribution of normalized order parameter $|\psi/\psi_\infty|$ obtained by a TDGL simulation with the temperature being 5.2 K (higher than $T_c^{impurity}$) and $B_{pk} = 50.9$ mT. This snapshot is taken at the end of an rf cycle, namely when the rf field drops to zero ($\omega t = 2\pi$ and hence $B_{rf} \sin(\omega t) = 0$). The normalized order parameter of the dark blue region is around 0.18.

The side view of the grain-boundary model is shown in Fig. 10, and the top view [$(x, y, z = 0)$] is shown in Fig. 11. Figure 11(a) is an illustration of an Nb surface containing Nb grains (red) and grain boundaries filled with low-T_c impurity phases (blue). The realization used in the TDGL simulations is shown in Fig. 11(b). Figure 11(b) is a top view of the sample critical temperature distribution around the origin of the grain-boundary model: the red region means Nb with $T_c = 9.3$ K, and the blue region means the low-T_c impurity phase with $T_c^{impurity} = 3$ K. (Parameters of the grain-boundary model are given in Appendix F and in Table V.) The origin is at the center of Fig. 11(b). The geometry is intentionally asymmetric in both the x direction and the y direction to prevent symmetry-induced artifacts. A top view of the sample-critical temperature distribution with a broader scope (containing the defect region together with the bulk Nb region) is shown in Appendix G.

An rf vortex semiloop that nucleates in the sample tends to be parallel to the direction of the rf dipole, which points in the x direction. Therefore, as $B_{pk} > B_{vortex}^{rf}(T)$, rf vortex semiloops show up in the grain boundaries that are roughly parallel to the x direction. Note that there is one grain boundary in Fig. 11(b) that is roughly parallel to the x direction and it is marked by a white dashed curve.

It is worth mentioning that the proximity effect shows up naturally in TDGL simulations. Figure 11(c) shows a snapshot of the distribution of normalized order parameter $|\psi/\psi_\infty|$ (here 1 means full superconductivity and 0 means no superconductivity) obtained by a TDGL simulation with the temperature being 5.2 K and $B_{pk} = 50.9$ mT. This snapshot is taken at the end of an rf cycle, namely when the rf field drops to zero ($\omega t = 2\pi$ and hence $B_{rf} \sin(\omega t) = 0$). Due to the proximity effect, the normalized order parameter of the dark blue region is around 0.18 but not zero, even though the temperature (5.2 K) is higher than $T_c^{impurity}$ (3 K). As a result, a grain boundary filled with a low-T_c impurity phase can host rf vortices even for $T > T_c^{impurity}$.

Figure 12 shows the simulation result of $P_{3f}(T)$ for the grain-boundary model shown in Fig. 10 (side view of the

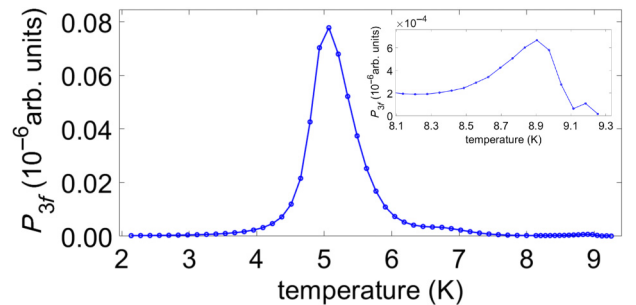FIG. 12. TDGL simulation result of $P_{3f}(T)$ for the grain-boundary model shown in Figs. 10 and 11. Here $h_{penetration}^{defect} = 200$ nm and $B_{pk} = 50.9$ mT. Inset: enlargement of the figure above 8.1 K.

the origin characterizes the grain-boundary scenario accurately (the model defect region), and thus the screening current is collected only from this region when calculating P_{3f}.
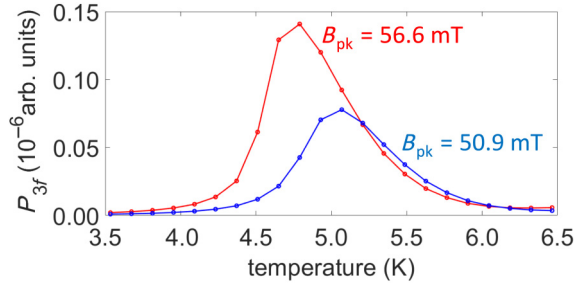
FIG. 13.   TDGL simulation result of $P_{3f}(T)$ for two different rf field amplitudes for the grain-boundary model shown in Figs. 10 and 11. Here $h_{penetration}^{defect} = 200$ nm.

model) and Fig. 11 (top view of the model). Compared to the P_{3f} around 8.9 K, the P_{3f} between 4.5 and 6 K is much stronger. In other words, in the presence of surface defects, P_{3f} generated by surface defects is much stronger than the intrinsic P_{3f} of Nb. In the following, we focus on the P_{3f} generated by surface defects.

Figure 13 shows the simulation result of $P_{3f}(T)$ for two different rf field amplitudes for the grain boundary model. At low temperatures, the sample is in the Meissner state and P_{3f} is weak. As temperature increases, rf vortex semiloops nucleate in the grain boundary marked by the white dashed curve in Fig. 11(b) and result in strong P_{3f}. (The existence of rf vortex semiloops is verified by examining the order parameter in a time-domain manner as described in Fig. 7.) This can be interpreted as $B_{pk} > B_{vortex}^{rf}(T)$, where $B_{vortex}^{rf}(T)$ is the vortex penetration field of the region around that specific grain boundary. Note that rf vortex semiloops show up in the grain boundary, indicating that the grain boundary serves as the weak spot for rf vortex nucleation. Video 2 shows the nucleation, movement, and exit of the rf vortex semiloop in the grain-boundary model in one rf cycle. The parameter setting can be found within the Supplemental Material [85].

Here the upper onset temperature of P_{3f} is around 6 K. The grain-boundary model is a mixture of the $T_c^{Nb} = 9.3$ K
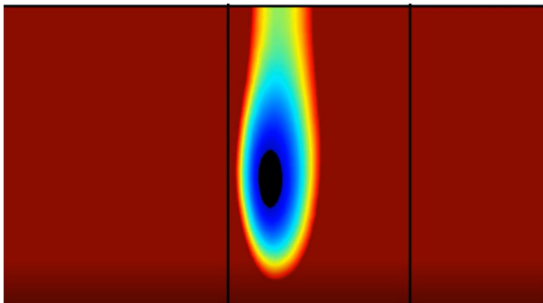
VIDEO 2.   An animation showing the nucleation, movement, and exit of the rf vortex semiloop in the grain-boundary model in one rf cycle.

Nb and the $T_c^{impurity} = 3$ K impurity phase, and hence T_c^{P3f} is between 3 and 9.3 K. Of course, the numerical value of T_c^{P3f} depends on how the Nb and the impurity phase are distributed. Our objective with this model is not to propose a specific microstructure of the sample, but to illustrate the generic nonlinear properties of a proximity-coupled defective region of the sample.

Similar to the case of bulk Nb [Fig. 9(a)], $P_{3f}(T)$ in Fig. 13 also exhibits the four key features (Table I). Therefore, the ideas illustrated in Fig. 9(b) could describe the physics of the grain-boundary model, with T_c^{P3f} being 6 K but not 9.3 K and $B_{vortex}^{rf}(T)$ being the vortex penetration field of the region around the specific grain boundary, but not a bulk property. The fact that experimental data (Figs. 4 and 6) and TDGL simulation of the grain-boundary model (Fig. 13) both exhibit the four key features (Table I) and a T_c^{P3f} below 9.3 K suggests that "rf vortex semiloops nucleate in grain boundaries hosting low-T_c impurity phases" is indeed one of the possible mechanisms of the observed P_{3f} signals for the HiPIMS Nb/Cu samples.

D. Effect of $h_{penetration}^{defect}$ on $P_{3f}(T)$

In Sec. IV C, $h_{penetration}^{defect}$ is set to be 200 nm. Here we consider the effect of varying $h_{penetration}^{defect}$, with everything else being the same as described in Sec. IV C.

Figure 14(a) shows the result for $h_{penetration}^{defect} = 160$ nm. Figure 14(a) is similar to the data in Fig. 6(a), in the sense that a stronger rf field amplitude leads to a stronger P_{3f} for all temperatures; Fig. 13 ($h_{penetration}^{defect} = 200$ nm) is similar to the data in Fig. 6 (b), in the sense that $P_{3f}(T)$ shows a "crossing" effect: a stronger rf field amplitude leads to a weaker P_{3f} (the red curve is below the blue curve) for temperatures close to T_c^{P3f}. The temperature where the red curve ($P_{3f}(T)$ with a strong rf field amplitude) and the blue curve ($P_{3f}(T)$ with a weak rf field amplitude) cross is denoted as T^*. The numerical value of T^* depends on the choice of the two rf field amplitudes (Here $B_{pk} = 56.6$ and 50.9 mT.) For Fig. 14(a), there is no crossing and hence $T^* = T_c^{P3f} = 6$ K. For Fig. 13, $T^* = 5.2$ K $< T_c^{P3f} = 6$ K. Figure 14(b) shows how the crossing temperature T^* changes with $h_{penetration}^{defect}$. For a small $h_{penetration}^{defect}$, there is no crossing and hence $T^* = T_c^{P3f}$. The crossing shows up when $h_{penetration}^{defect}$ is beyond a critical depth. As $h_{penetration}^{defect}$ becomes larger, the crossing effect becomes more significant (T^* becomes smaller, which means that the temperature window that a stronger rf field amplitude leads to a weaker P_{3f} becomes larger) and eventually tends to saturate.

The crossing effect can be understood as follows. In experiments and simulations, P_{3f} is collected by the magnetic writer, and in the simulations at the rf dipole location, which is at $z = h_{dp}$ (above the sample surface). For a weak rf field amplitude, the rf vortex semiloop in the grain boundary stays close to the sample surface ($z = 0$). As
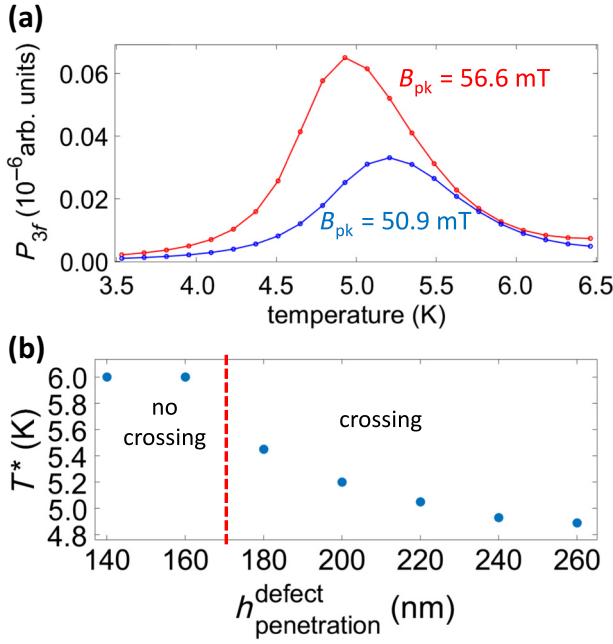
FIG. 14. (a) TDGL simulation result of $P_{3f}(T)$ for two different rf field amplitudes for the grain-boundary model shown in Figs. 10 and 11 for $h_{\text{penetration}}^{\text{defect}} = 160$ nm. (b) Crossing temperature T^* as a function of $h_{\text{penetration}}^{\text{defect}}$.

FIG. 15. A grain-boundary model containing two grain boundaries that are roughly parallel to the x direction. (a) The distribution of critical temperature on the X-Y plane around the origin, with red being Nb and blue being the low-T_c impurity phase with $T_c^{\text{impurity}} = 3$ K. Here $(x, y, z) = (0, 0, 0)$ is at the center. The rf dipole is located at $(x, y, z) = (0, 0, 400$ nm$)$, which is above the center of the image, and points in the x direction. The two white dashed curves indicate the grain boundaries (the top grain boundary and the bottom grain boundary) that are roughly parallel to the x direction. The model defect region is indicated by the white dashed circle. (b) TDGL simulation result of $P_{3f}(T)$ for the grain-boundary model shown in (a). Here $h_{\text{penetration}}^{\text{defect}} = 280$ nm, and $B_{\text{pk}} = 50.9$ mT.

the rf field amplitude increases, the rf vortex semiloop in the grain boundary is pushed toward the bottom of the grain boundary that it can penetrate ($z = -h_{\text{penetration}}^{\text{defect}}$) (see Appendix H for a visualization of this effect), which means that the rf vortex semiloop is farther away from the magnetic writer and the rf dipole location ($z = h_{\text{dp}}$), and hence the measured P_{3f} becomes weaker. Such a phenomenon shows up only when the rf vortex semiloop in the grain boundary can be pushed far away from the sample surface. For a small $h_{\text{penetration}}^{\text{defect}}$, the rf vortex semiloop always stays just below the sample surface instead of penetrating deep into the sample, and hence P_{3f} does not decrease as the rf field amplitude increases (no crossing effect).

Note that the results presented in Fig. 14 are obtained using the grain-boundary model, which is meant to be a phenomenological toy model. Therefore, the numerical values of $h_{\text{penetration}}^{\text{defect}}$ should not be interpreted literally. The key insight here is that there is no crossing effect for a small $h_{\text{penetration}}^{\text{defect}}$ (shallow penetration), and the crossing effect becomes apparent for a large $h_{\text{penetration}}^{\text{defect}}$ (deep penetration).

E. Simulation of a defect model with two grain boundaries

In the grain-boundary model discussed in Secs. IV C and IV D, there is only one single grain boundary underneath and roughly parallel to the rf dipole, and thus rf vortex semiloops nucleate in one single grain boundary and $P_{3f}(T)$ shows a single-peak feature. Such a scenario
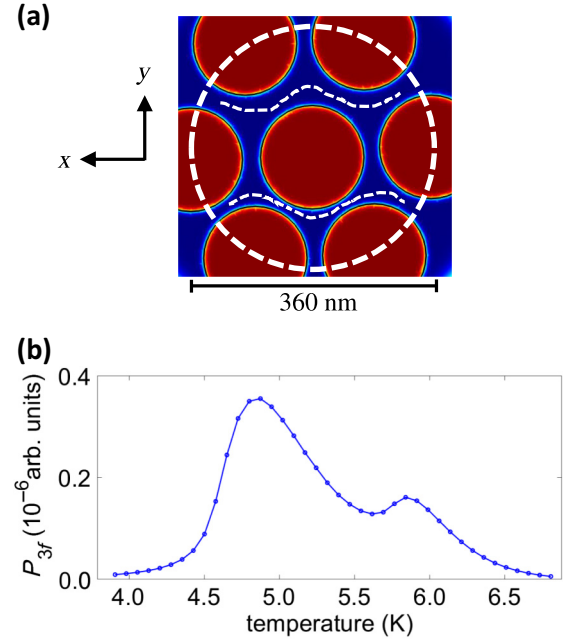
corresponds to the case where the density of the sample grain boundaries that nucleates rf vortices (ρ^{defect}) is low. For a sample with a high density of grain boundaries that nucleates rf vortices, it can be modeled as a grain-boundary model that contains two grain boundaries underneath and roughly parallel to the rf dipole.

Here we consider a grain-boundary model that contains two grain boundaries that are near the origin and roughly parallel to the x direction. The basic setting of the model is the same as described in Sec. IV C. The only difference is how the Nb and the impurity phase are distributed horizontally, as shown in Fig. 15(a). Figure 15(a) shows the top view of the critical temperature distribution and Fig. 15(b) shows the TDGL simulation result of $P_{3f}(T)$ for this model.

The two-peak feature of $P_{3f}(T)$ in Fig. 15(b) can be understood as follows. At low temperatures, the sample is in the Meissner state and P_{3f} is weak. As temperature increases, around 4.50 K an rf vortex semiloop nucleates in the top grain boundary and results in the lower temperature peak, and then around 5.77 K another rf vortex semiloop

nucleates in the bottom grain boundary and results in the higher-temperature peak. That is, rf vortex semiloops nucleate in both grain boundaries and thus result in the two-peak feature of $P_{3f}(T)$. The nucleation of the two rf vortex semiloops is verified by monitoring $\Delta\theta/2\pi$ (the same analysis as shown in Fig. 8). Note that the two-peak feature of the $P_{3f}(T)$ in Fig. 15(b) (simulation) is also observed in Fig. 4 (measurement).

F. Nb/Cu samples comparison

Larger values of P_{3f} are closely related to the presence of rf vortex semiloops. By studying P_{3f}, we investigate surface defects that nucleate rf vortex semiloops, which are the kinds of surface defects that are closely related to the rf performance of SRF cavities. In the following, surface defects refer to the kind of surface defects that nucleate rf vortex semiloops.

Equipped with the simulation results, the measured P_{3f} can be analyzed further. First, the number of $P_{3f}(T)$ peaks can be related to the density of surface defects (ρ^{defect}). Single-peak $P_{3f}(T)$ corresponds to a low density of surface defects, and two-peak $P_{3f}(T)$ corresponds to a high density of surface defects. Second, the crossing effect of $P_{3f}(T)$ can be related to how deep an rf vortex semiloop penetrates into a sample through a surface defect ($h_{\text{penetration}}^{\text{defect}}$). The absence of the crossing effect corresponds to a small $h_{\text{penetration}}^{\text{defect}}$ (shallow), and the presence of the crossing effect corresponds to a large $h_{\text{penetration}}^{\text{defect}}$ (deep).

The assignment of qualitative surface defect properties of all seven Nb/Cu samples is summarized in Table III. The second column shows an estimate for the density of surface defects that nucleate rf vortex semi-loops (ρ^{defect}) and the third column shows how deep an rf vortex semiloop penetrates into a sample through a surface defect ($h_{\text{penetration}}^{\text{defect}}$). rf vortex penetration through surface defects is one of the main enemies of SRF applications. To achieve good SRF performance, the surface defect density should be low and the defect should be shallow. From the perspective of these

two properties, among the five HiPIMS Nb/Cu samples with nonzero voltage bias, the HiPIMS 75-V bias Nb/Cu sample is the most effective in reducing the nucleation of rf vortices associated with surface defects.

In the numerical simulations of this work, surface defects that nucleate rf vortex semiloops are modeled as grain boundaries. Since P_{3f} is associated with the behavior of rf vortex semiloops, it is likely that the ideas of ρ^{defect} and $h_{\text{penetration}}^{\text{defect}}$ could apply to surface defects other than grain boundaries (dislocations, for example).

For the DCMS sample, the actual P_{3f} value of the sample response remains unknown due to interference with the background signal and the lack of relative phase information [see Fig. 16(d) and related discussion in Appendix B]. Consequently, the TDGL simulation results cannot be directly applied to the experimental data of the DCMS sample.

V. CONCLUSION

In this work, we study seven Nb/Cu films that are candidates for SRF applications. Local P_{3f} measurements reveal surface defects with P_{3f} onset temperatures between 6.3 and 6.8 K for five out of the six HiPIMS Nb/Cu samples, indicating that such defects are a generic feature of these air-exposed HiPIMS Nb/Cu films. The signal from the low-T_c surface defect is much stronger than the intrinsic Nb response around 9 K, suggesting that our local P_{3f} measurement is sensitive to surface defects. With the capability of μm-scale scanning, it is found that such a defect is quite uniform in space on the μm scale.

TDGL simulations are performed to analyze the experimental results further. In particular, the simulations suggest that the density of surface defects that nucleate rf vortices and how deep rf vortices travel through these surface defects can be extracted qualitatively from our local P_{3f} measurements. From the point of view of these two properties, the HiPIMS 75-V bias Nb/Cu sample stands out as the most effective in reducing the nucleation of rf vortices associated with surface defects.

APPENDIX A: SAMPLE PREPARATION

Here we discuss how the seven Nb/Cu films studied in this paper are prepared.

TABLE III. Comparison of the seven Nb/Cu samples. The second column shows qualitative assignments of the density of surface defects that nucleate rf vortex semiloops (ρ^{defect}) and the third column shows qualitative assignments of how deep an rf vortex semiloop penetrates into a sample through a surface defect ($h_{\text{penetration}}^{\text{defect}}$).

Sample	ρ^{defect}	$h_{\text{penetration}}^{\text{defect}}$
HiPIMS, 125-V bias	low	deep
HiPIMS, 100-V bias	low	deep
HiPIMS, 75-V bias	low	shallow
HiPIMS, 50-V bias	high	shallow
HiPIMS, 25-V bias	high	shallow
HiPIMS, no bias	N/A	
DCMS, no bias	N/A	

The substrate used for the Nb coatings is a 2-mm-thick, oxygen-free electronic (OFE) copper disk measuring 75 mm in diameter. Prior to coating, the substrate disk is degreased using commercial detergent. The sample is then chemically polished using a mixture of sulfamic acid (H_3NSO_3, 5 g/l), hydrogen peroxide (H_2O_2, 5% vol.), *n*-butanol (5% vol.) and ammonium citrate (1 g/l) heated up at 72 °C for 20 min. After polishing, the disk is rinsed with sulfamic acid to remove the buildup of native oxide and cleaned with deionized water and ultrapure ethanol.

The Cu substrate is mounted on an ultrahigh vacuum (UHV) stainless-steel chamber equipped with a rotatable shutter to expose in turn the areas to be coated, and the chamber is then connected to a sputtering system. Both assemblies are performed inside an ISO5 cleanroom, and the sputtering apparatus is described in detail in Ref. [62]. The entire system is transported to the coating bench where it is coupled to the pumping group and gas-injection lines, and pumped down to about 1×10^{-7} mbar. The pumping group and the sputtering system undergo a 48-h bakeout at 200 °C, during which a 4-hour activation of the nonevaporable getter (NEG) pump is performed. The temperature of the UHV chamber is maintained at 150 °C until the start of the coating. After cooling down, the system reaches a base pressure around 9.3×10^{-10} mbar. Ultrapure krypton (99.998%) is injected into the system until a process pressure of 2.3×10^{-3} mbar is reached. The seven coatings are then performed according to the deposition parameters outlined in Table IV. One of the samples is prepared by direct current magnetron sputtering with zero bias, and the coating thickness is around 3.5 µm. The other six samples are prepared by high-power impulse magnetron sputtering, with bias voltages ranging from 0 to −125 V, with coating thicknesses ranging from 1.15 to 1.5 µm.

During the coating process, the sample temperature was monitored with an infrared thermal sensor (OMEGA OS100-SOFT) and kept constant at 150 °C. The HiPIMS plasma discharge was maintained using a pulsed power supply (Huettinger TruPlasma HighPulse 4006) and the negative bias voltage was applied to the samples using a dc power supply (TruPlasma Bias 3018). The DCMS discharge was maintained using a Huettinger Truplasma 3005

power supply. The discharge and bias voltages and currents were monitored throughout the entire coating process using voltage (Tektronix P6015A) and current (Pearson current monitor 301×) probes whose signals are recorded by a digital oscilloscope (Picoscope 2000). After the coating, the samples were cooled down to room temperature, after which the chamber was vented with dry air. The Nb layer thickness is measured by x-ray fluorescence via the attenuation method.

APPENDIX B: DATA FOR TWO HIPIMS SAMPLES AND THE DCMS SAMPLE

Here we show the representative data for $P_{3f}(T)$ generated by surface defects for the HiPIMS 50-V bias sample, the HiPIMS 100-V bias sample, and the DCMS sample. For the HiPIMS 50-V bias sample, $P_{3f}(T)$ with T_c^{P3f} around 6.4 K is observed in a strong input-power regime [Fig. 16(a)], and $P_{3f}(T)$ with T_c^{P3f} around 6.8 K is observed in a weak input power regime [Fig. 16(b)]. For the HiPIMS 100-V bias sample, $P_{3f}(T)$ with T_c^{P3f} around 6.5 K is observed [Fig. 16(c)].

For the DCMS sample, $P_{3f}(T)$ with T_c^{P3f} around 6.5 K is observed [Fig. 16(d)]. The measured P_{3f} is the superposition of the probe background and the sample response. Consequently, the total signal may be weaker than the probe background if these two components are out of phase. In the absence of phase information, we simply subtract the probe background from the total signal in a scalar manner. This naive background subtraction can lead to negative P_{3f} values, as observed in Fig. 16(d) for $T < 6.5$ K.

The phase information can be obtained by conducting measurements with a vector network analyzer [51,53], which provides both amplitude and phase data, instead of a spectrum analyzer that measures only amplitude. However, due to its superior noise floor (approximately −155 dBm), we chose to use a spectrum analyzer for this work, rather than a vector network analyzer, which has a noise floor of around −130 dBm.

APPENDIX C: DATA FOR THE HIPIMS NO BIAS SAMPLE

Here we discuss the data of the HiPIMS 0-V bias Nb/Cu sample, as shown in Fig. 17. For this sample, $P_{3f}(T)$ shows a clear transition around 9 K. In addition to the intrinsic Nb response, $P_{3f}(T)$ demonstrates a nontrivial temperature dependence around 7.6 and 6.5 K, indicating the presence of surface defects.

The surface-defect signal of the HiPIMS 0-V bias Nb/Cu sample is qualitatively different from all the other samples examined in this work in two aspects. First, $P_{3f}(T)$ shows a bell-shaped structure in all the other samples (see Figs. 4, 6 and 16). Second, in all other samples that display

TABLE IV. Sample preparation parameters of the seven Nb/Cu films studied in this paper.

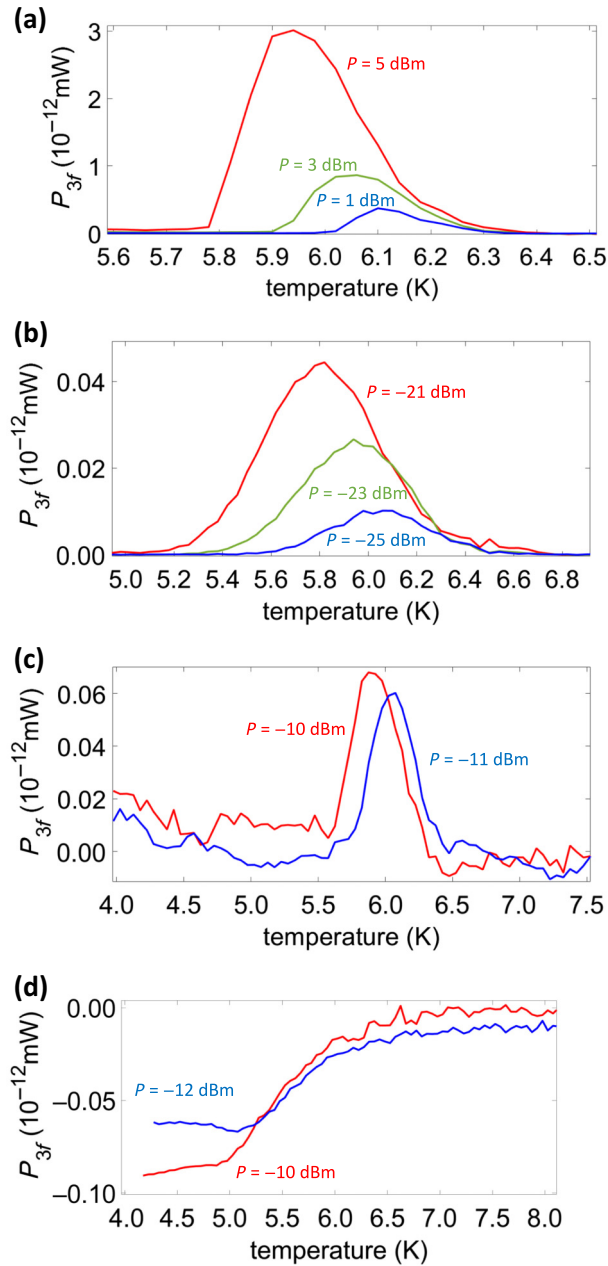| Parameter	HiPIMS	DCMS
Average power (kW)	1.3	1.3
Discharge voltage (V)	−600	−377
Current (A)	160 (peak current)	3.4
Working gas	Kr	Kr
Pressure (mbar)	2.3×10^{-3}	2.3×10^{-3}
Temperature (°C)	150	150
Coating duration (min)	60	60

FIG. 16. (a),(b) show $P_{3f}(T)$ for the HiPIMS 50-V bias Nb/Cu sample with an input frequency of 2.16 GHz in a strong input-power regime and in a weak input-power regime, respectively. (c) shows $P_{3f}(T)$ for the HiPIMS 100-V bias Nb/Cu sample with an input frequency of 1.18 GHz. (d) shows $P_{3f}(T)$ for the DCMS Nb/Cu sample with an input frequency of 1.22 GHz. The negative value for $T < 6.5$ K is discussed in the second paragraph of Appendix B.
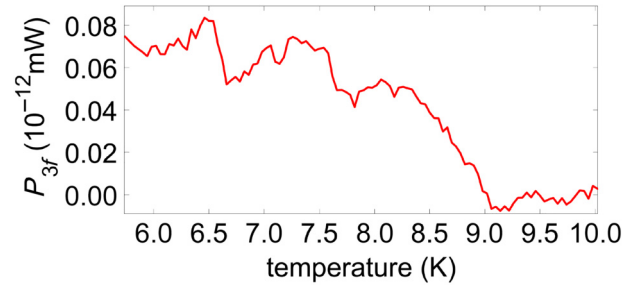

FIG. 17. Measured $P_{3f}(T)$ for the HiPIMS 0-V bias Nb/Cu sample. The input frequency is 1.98 GHz and the input power is 3 dBm.

the HiPIMS 0-V samples show significant porosity inside the film, which is quite different from all other HiPIMS films at nonzero bias [62]. This porosity may give rise to a qualitatively different type of nonlinear response, which is beyond the scope of the present work.

APPENDIX D: COMPARISON WITH OUR PREVIOUS RESEARCH

In our previous research [57], we explored the third-harmonic response of several bulk Nb samples and Nb/Cu films with the same experimental setup described in this work. Here we briefly compare the main difference between our previous research [57] and this study.

For the simulation part, Ref. [57] adopts a hybrid approach: the third-harmonic response from surface defects is analyzed with the Josephson-junction model, which is a circuit model, while the third-harmonic response from rf vortex semiloop nucleation in (defect-free) Nb is analyzed with TDGL simulations. In contrast, surface defects and Nb are both analyzed with the TDGL framework in this work (see Sec. IV C).

For the experiment part, the periodic feature observed in Ref. [57] (explained by the Josephson-junction model) is absent in the Nb/Cu films studied in this work. This suggests that the old-generation samples and the new-generation samples might have different kinds of surface defects. Consequently, instead of using the Josephson-junction model, we explore a different surface-defect model in this work, namely the grain-boundary model (see Sec. IV C).

APPENDIX E: CHECK FOR HYSTERESIS IN P_{3f} MEASUREMENTS

Here we check whether or not $P_{3f}(T)$ measurements exhibit hysteresis. The HiPIMS 125-V bias Nb/Cu sample first undergoes a cool down from 10 to 3.6 K with zero rf field. The microwave signal is turned on after the temperature stabilizes at 3.6 K. The sample then gradually warms up from 3.6 to 10 K [warm-up $P_{3f}(T)$], and then cools down from 10 to 3.6 K [cool-down $P_{3f}(T)$],

both responses, the surface-defect signal is much stronger than the intrinsic Nb response (see Fig. 3). Consequently, the HiPIMS 0-V bias Nb/Cu sample likely exhibits a unique mechanism generating nonlinearity, distinct from the mechanisms observed in all the other six samples. Notably, when deposited on complex-shaped substrates,
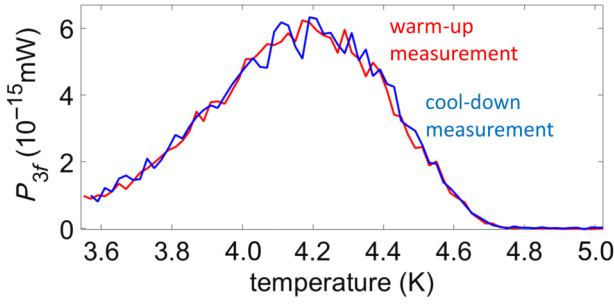
FIG. 18. Check for hysteresis in $P_{3f}(T)$ measurement for the HiPIMS 125-V bias Nb/Cu sample. The input frequency is 1.88 GHz and the input power is -25 dBm.

with the microwave signal being turned on in this process. As shown in Fig. 18, such $P_{3f}(T)$ measurement does not exhibit a clear hysteresis.

The measurement of Fig. 18 is performed one year and a half after the measurement of Fig. 6(b). It is quite likely that different regions of the sample surface are studied in these two measurements. This might explain why Fig. 18 ($T_c^{P3f} = 4.8$ K) and Fig. 6(b) ($T_c^{P3f} = 6.8$ K) show different P_{3f} signals.

APPENDIX F: EQUATIONS AND PARAMETERS FOR TDGL SIMULATIONS

In TDGL, the relaxation dynamics of the order parameter ψ is assumed to be described as follows [86,92]:

$$-\gamma \left(\frac{\partial}{\partial t} + i\frac{e_*}{\hbar}\Phi \right)\psi = \frac{\delta F_{GL}}{\delta \psi^*}, \tag{F1}$$

with the Ginzburg-Landau free energy F_{GL} given by

$$F_{GL} = \frac{-1}{2m_*}|(-i\hbar\nabla - e_*A)\psi|^2 + \alpha|\psi|^2 + \frac{\beta}{2}|\psi|^4$$
$$+ \frac{1}{2\mu_0}|\nabla \times A - B_{ext}|^2. \tag{F2}$$

Here $e_* = 2e$ is the charge of the Cooper pair, $m_* = 2m_e$ is the mass of the Cooper pair, Φ is the electric potential, $\gamma = \pi\hbar|\alpha|/8k_B(T_c - T)$ plays the role of a friction coefficient, ψ is the order parameter, A is the total vector potential (arising from both external and self-generated sources), B_{ext} is the external magnetic field, and both α and β are material-specific phenomenological parameters. The dynamics of ψ and the electromagnetic field are described by Maxwell's equations and the following TDGL equations:

$$\gamma \left(\frac{\partial}{\partial t} + i\frac{e_*}{\hbar}\Phi \right)\psi = \frac{-1}{2m_*}(-i\hbar\nabla - e_*A)^2\psi$$
$$- \alpha\psi - \beta|\psi|^2\psi \tag{F3}$$

and

$$\sigma \left(\nabla\Phi + \frac{\partial A}{\partial t} \right) = \frac{-i\hbar e_*}{2m_*}(\psi^*\nabla\psi - \psi\nabla\psi^*) - \frac{e_*^2}{m_*}|\psi|^2 A$$
$$- \frac{1}{\mu_0}\nabla \times (\nabla \times A - B_{ext}). \tag{F4}$$

Here σ is the electric conductivity of the normal state.

The Ginzburg-Landau order parameter relaxation time τ_{GL} is given by

$$\tau_{GL} = \frac{\pi\hbar}{8k_B(T_c - T)} = (3 \times 10^{-12} \text{ s}) \left(\frac{K}{T_c - T} \right). \tag{F5}$$

The dynamics of a superconductor when driven by an rf field of a few GHz is in the adiabatic limit unless T is extremely close to T_c ($T_c - T < 10^{-2}$ K).

There is no external current inside the superconductor in our setup, and hence $\nabla \times B_{ext} = \mu_0 J_{ext} = 0$ inside the superconductor. In addition, we choose the gauge such that the scalar potential is zero, namely $\Phi = 0$. The two TDGL equations inside the superconductor become

$$\gamma \frac{\partial\psi}{\partial t} = \frac{-1}{2m_*}(-i\hbar\nabla - e_*A)^2\psi - \alpha\psi - \beta|\psi|^2\psi \tag{F6}$$

and

$$\sigma \frac{\partial A}{\partial t} = \frac{-i\hbar e_*}{2m_*}(\psi^*\nabla\psi - \psi\nabla\psi^*) - \frac{e_*^2}{m_*}|\psi|^2 A$$
$$- \frac{1}{\mu_0}\nabla \times \nabla \times A. \tag{F7}$$

Note that α and β, namely the two material-specific phenomenological parameters of the Ginzburg-Landau free energy, can be related to the penetration depth λ and the thermodynamic critical field B_c by

$$\lambda = \sqrt{\frac{m_*\beta}{\mu_0 e_*^2 |\alpha|}} \tag{F8}$$

and

$$B_c = \frac{\sqrt{\mu_0}|\alpha|}{\sqrt{\beta}}. \tag{F9}$$

In the two surface-defect models (Secs. IV C–IV E), the superconducting samples contain Nb and the low-T_c impurity phase, and thus are inhomogeneous. Equations (F6) and (F7) are applied to both the Nb region and the low-T_c impurity phase region, and the inhomogeneity is incorporated via the spatial variation of the five material-specific parameters T_c, α, β, γ, and σ. In practice, the values of α and β are obtained for a given choice of λ and B_c through Eqs. (F8) and (F9).

TABLE V.　Values of parameters used in TDGL simulations for bulk Nb (Sec. IV B) and for the two surface-defect impurity models (Secs. IV C–IV E).

Parameter name		Symbol	Value
Dipole height		h_{dp}	400 nm
Period of applied rf field		$1/f$	5.88×10^{-10} s
Nb	Critical temperature	T_c^{Nb}	9.3 K
	Penetration depth	λ^{Nb}	40 nm
	Critical field	B_c^{Nb}	200 mT
impurity	Critical temperature	$T_c^{impurity}$	3.0 K
	Penetration depth	$\lambda^{impurity}$	90 nm
	Critical field	$B_c^{impurity}$	120 mT

Material parameters (penetration depth λ, Ginzburg-Landau parameter κ, etc.) of Nb films vary from one sample to another. For the Nb part in the TDGL simulations, we adopt the material parameters of bulk Nb as shown in the first row of Table 1 of Ref. [58] for simplicity.

We now discuss the choice of the material parameters of the low-T_c impurity phase in the two surface-defect models. For simplicity, the normal-state conductivity of the low-T_c impurity phase is set to be the same as that of Nb. The transition temperature of the low-T_c impurity phase is set to be 3 K. The penetration depth of the low-T_c impurity phase is expected to be larger than that of Nb (40 nm) and is set to be 90 nm; the thermodynamic critical field of the low-T_c impurity phase is expected to be smaller than that of Nb (200 mT) and is set to be 120 mT. Values of parameters used in TDGL simulations are summarized in Table V. The "impurity" sector specifies the material parameters of the low-T_c impurity phase region in the two surface-defect models (Secs. IV C–IV E).

To numerically simulate the superconducting domain, boundary conditions need to be specified. Any current passing through the boundary between a superconductor and a vacuum is unphysical, and hence on the boundary $\partial\Omega$ of a superconducting domain we expect [79]

$$J \cdot \hat{n} = 0 \quad \text{on } \partial\Omega. \quad (F10)$$

Here $\hat{n}$ is the unit vector normal to the boundary. The supercurrent J_s is given by

$$J_s = \frac{-i\hbar e_*}{2m_*}\left(\psi^*\nabla\psi - \psi\nabla\psi^*\right) - \frac{e_*^2}{m_*}|\psi|^2 A. \quad (F11)$$

The boundary condition, Eq. (F10), should hold even when $A = 0$, and thus the boundary condition (F10) becomes

$$\nabla\psi \cdot \hat{n} = 0 \quad \text{on } \partial\Omega. \quad (F12)$$

Combine Eqs. (F10)–(F12) and we obtain

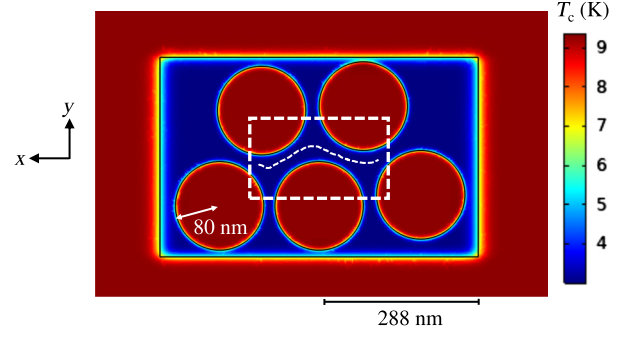$$A \cdot \hat{n} = 0 \quad \text{on } \partial\Omega. \quad (F13)$$

FIG. 19.　A spatially extended view of the distribution of critical temperature on the X-Y plane for the grain-boundary model discussed in Sec. IV C. The region shown here corresponds to the region indicated by the green dashed line in Fig. 10.

Equations (F12) and (F13) are applied as the boundary conditions of the superconductor-vacuum interface.

APPENDIX G: A TOP VIEW FOR THE GRAIN-BOUNDARY MODEL IN SEC. IV C

Figure 11(b) shows the region around the origin (which plays the dominant role in rf vortex nucleation and P_{3f}) for the grain-boundary model discussed in Sec. IV C. Compared to Fig. 11(b), Fig. 19 shows the setup over a broader spatial extent as indicated by the green dashed line in Fig. 10. Figure 19 contains the entire defect region (the
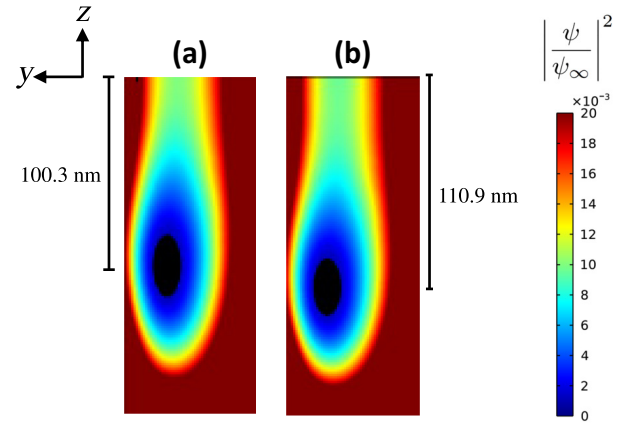

FIG. 20.　A snapshot of the vortex core obtained by the TDGL simulation for the grain-boundary model in Sec. IV C for $B_{pk} = 50.9$ mT (a) and for $B_{pk} = 56.6$ mT (b), with the temperature being 5.5 K and $h_{penetration}^{defect} = 200$ nm. This snapshot is taken when the rf field reaches its maximum in an rf cycle [$\omega t = \pi/2$ and hence $B_{rf}\sin(\omega t) = B_{rf}$]. The snapshot shows the distribution of the square of the normalized order parameter on the Y-Z plane immediately below the dipole around the grain boundary that nucleates an rf vortex semiloop. The black region is where $|\psi/\psi_\infty|^2 < 0.001$.

five Nb grains and the blue region) and part of the bulk Nb region as shown in Fig. 10.

APPENDIX H: SNAPSHOTS OF A VORTEX IN A GRAIN BOUNDARY FOR THE GRAIN-BOUNDARY MODEL IN SEC. IV C

An rf vortex semiloop is roughly parallel to the direction of the rf dipole, which points in the x direction, and hence the cross section of the rf vortex semiloop is on the Y-Z plane. Figure 20 visualizes an rf vortex semiloop in the grain boundary marked by the white dashed curve in Fig. 11(b), with the vortex core corresponding to the black region, where $|\psi/\psi_\infty|^2 < 0.001$. The rf vortex semiloop penetrates the sample surface and the vortex core is around 100.3-nm deep for $B_{pk} = 50.9$ mT [Fig. 20(a)] and is around 110.9-nm deep for $B_{pk} = 56.6$ mT [Fig. 20(b)].

---

[1] Hasan Padamsee, 50 years of success for SRF accelerators—A review, Supercond. Sci. Technol. **30,** 053003 (2017).

[2] Philip Bambade, Tim Barklow, Ties Behnke, Mikael Berggren, James Brau, Philip Burrows, Dmitri Denisov, Angeles Faus-Golfe, Brian Foster, Keisuke Fujii, *et al.*, The international linear collider: A global project, ArXiv:1903.01629.

[3] Gianluigi Ciovati, Review of the frontier workshop and Q-slope results, Physica C **441,** 44 (2006).

[4] A. Gurevich, Multiscale mechanisms of SRF breakdown, Physica C **441,** 38 (2006).

[5] Alex Gurevich, Superconducting radio-frequency fundamentals for particle accelerators, Rev. Accelerator Sci. Technol. **5,** 119 (2012).

[6] Alex Gurevich, Theory of RF superconductivity for resonant cavities, Supercond. Sci. Technol. **30,** 034004 (2017).

[7] Mark S. Champion, Lance D. Cooley, Camille M. Ginsburg, Dmitri A. Sergatskov, Rongli L. Geng, Hitoshi Hayano, Yoshihisa Iwashita, and Yujiro Tajima, Quench-limited SRF cavities: Failure at the heat-affected zone, IEEE Trans. Appl. Supercond. **19,** 1384 (2009).

[8] Shiran Bao and Wei Guo, Quench-spot detection for superconducting accelerator cavities via flow visualization in superfluid helium-4, Phys. Rev. Appl. **11,** 044003 (2019).

[9] S. Posen, N. Valles, and M. Liepe, Radio frequency magnetic field limits of Nb and Nb_3Sn, Phys. Rev. Lett. **115,** 047001 (2015).

[10] P. Kneisel, G. Ciovati, P. Dhakal, K. Saito, W. Singer, Xenia Singer, and G. R. Myneni, Review of ingot niobium as a material for superconducting radiofrequency accelerating cavities, Nucl. Instrum. Methods Phys. Res. Section A, **774,** 133 (2015).

[11] C. Z. Antoine, Influence of crystalline structure on rf dissipation in superconducting niobium, Phys. Rev. Accel. Beams **22,** 034801 (2019).

[12] Wolfgang Weingarten, Field-dependent surface resistance for superconducting niobium accelerating cavities-

condensed overview of weak superconducting defect model, IEEE Trans. Appl. Supercond. **33,** 3500309 (2023).

[13] Kevin E. Yoon, David N. Seidman, Claire Antoine, and Pierre Bauer, Atomic-scale chemical analyses of niobium oxide/niobium interfaces via atom-probe tomography, Appl. Phys. Lett. **93,** 132502 (2008).

[14] Th. Proslier, John F. Zasadzinski, L. Cooley, C. Antoine, J. Moore, J. Norem, M. Pellin, and K. E. Gray, Tunneling study of cavity grade Nb: Possible magnetic scattering at the surface, Appl. Phys. Lett. **92,** 212505 (2008).

[15] A. Romanenko and D. I. Schuster, Understanding quality factor degradation in superconducting niobium cavities at low microwave field amplitudes, Phys. Rev. Lett. **119,** 264801 (2017).

[16] Guilherme Dalla Lana Semione, A. Dangwal Pandey, S. Tober, J. Pfrommer, A. Poulain, J. Drnec, G. Schütz, T. F. Keller, H. Noei, V. Vonk, *et al.*, Niobium near-surface composition during nitrogen infusion relevant for superconducting radio-frequency cavities, Phys. Rev. Accel. Beams **22,** 103102 (2019).

[17] Guilherme Dalla Lana Semione, Vedran Vonk, Arti Dangwal Pandey, Elin Grånäs, Björn Arndt, Marc Wenskat, Wolfgang Hillert, Heshmat Noei, and Andreas Stierle, Temperature-dependent near-surface interstitial segregation in niobium, J. Phys.: Condens. Matter **33,** 265001 (2021).

[18] Roberto Russo, Quality measurement of niobium thin films for Nb/Cu superconducting RF cavities, Meas. Sci. Technol. **18,** 2299 (2007).

[19] Maxim Kharitonov, Thomas Proslier, Andreas Glatz, and Michael J. Pellin, Surface impedance of superconductors with magnetic impurities, Phys. Rev. B **86,** 024514 (2012).

[20] Jared Carlson, Alden Pack, Mark K. Transtrum, Jaeyel Lee, David N. Seidman, Danilo B. Liarte, Nathan S. Sitaraman, Alen Senanian, Michelle M. Kelley, James P. Sethna, *et al.*, Analysis of magnetic vortex dissipation in Sn-segregated boundaries in Nb_3Sn superconducting RF cavities, Phys. Rev. B **103,** 024516 (2021).

[21] P. J. Lee, A. A. Polyanskii, Zu-Hawn Sung, D. C. Larbalestier, C. Antoine, P. C. Bauer, C. Boffo, and H. T. Edwards, in *AIP Conference Proceedings* (American Institute of Physics, Ridge, NY, 2007), Vol. 927, pp. 113–120.

[22] A. A. Polyanskii, P. J. Lee, A. Gurevich, Zu-Hawn Sung, and D. C. Larbalestier, in *AIP Conference Proceedings* (American Institute of Physics, Ridge, NY, 2011), Vol. 1352, pp. 186–202.

[23] J. Köszegi, O. Kugeler, D. Abou-Ras, J. Knobloch, and R. Schäfer, A magneto-optical study on magnetic flux expulsion and pinning in high-purity niobium, J. Appl. Phys. **122,** 173901 (2017).

[24] Mingmin Wang, Shreyas Balachandran, Thomas Bieler, Santosh Chetri, Chris Compton, Peter Lee, and Anatolii Polyanskii, in *Proc. of International Conference on RF Superconductivity (SRF'17)* (JACoW, Geneva, Switzerland, 2018), pp. 787–791.

[25] Mingmin Wang, Anatolii Polyanskii, Shreyas Balachandran, Santosh Chetri, Martin A. Crimp, Peter J. Lee, and Thomas R. Bieler, Investigation of the effect of structural defects from hydride precipitation on superconducting properties of high purity SRF cavity Nb using

magneto-optical and electron imaging methods, Supercond. Sci. Technol. **35**, 045001 (2022).

[26] Jaeyel Lee, Zugang Mao, Kai He, Zu Hawn Sung, Tiziana Spina, Sung-Il Baik, Daniel L. Hall, Matthias Liepe, David N. Seidman, Sam Posen, *et al.*, Grain-boundary structure and segregation in Nb_3Sn coatings on Nb for high-performance superconducting radiofrequency cavity applications, Acta Mater. **188**, 155 (2020).

[27] A. Romanenko and H. Padamsee, The role of near-surface dislocations in the high magnetic field performance of superconducting niobium cavities, Supercond. Sci. Technol. **23**, 045008 (2010).

[28] T. R. Bieler, N. T. Wright, F. Pourboghrat, C. Compton, K. T. Hartwig, D. Baars, A. Zamiri, S. Chandrasekaran, P. Darbandi, H. Jiang, *et al.*, Physical and mechanical metallurgy of high purity Nb for accelerator cavities, Phys. Rev. Spec. Top.-Accel. Beams **13**, 031002 (2010).

[29] Qing-Yu Wang, Cun Xue, Chao Dong, and You-He Zhou, Effects of defects and surface roughness on the vortex penetration and vortex dynamics in superconductor–insulator–superconductor multilayer structures exposed to RF magnetic fields: Numerical simulations within TDGL theory, Supercond. Sci. Technol. **35**, 045004 (2022).

[30] R. Ries, E. Seiler, F. Gömöry, A. Medvids, C. Pira, and O. B. Malyshev, in *Journal of Physics: Conference Series* (IOP Publishing, Bristol, UK, 2020), Vol. 1559, p. 012040.

[31] Pashupati Dhakal, Gianluigi Ciovati, Peter Kneisel, and Ganapati Rao Myneni, Enhancement in quality factor of SRF niobium cavities by material diffusion, IEEE Trans. Appl. Supercond. **25**, 1 (2014).

[32] Dan Gonnella and Matthias Liepe, in *Proceedings of the LINAC 2014, MOPP017* (JaCoW, Geneva, Switzerland, 2014), pp. 84–87, https://inspirehep.net/literature/1363314.

[33] Raphael Kleindienst, Andrew Burrill, Oliver Kugeler, and Jens Knobloch, Commissioning results of the HZB quadrupole resonator, Tech. Rep., https://cds.cern.ch/record/2058158, 2015.

[34] S. Keckert, R. Kleindienst, O. Kugeler, D. Tikhonov, and J. Knobloch, Characterizing materials for superconducting radiofrequency applications—A comprehensive overview of the quadrupole resonator design and measurement capabilities, Rev. Sci. Instrum. **92**, 064710 (2021).

[35] Marco Arzeo, F. Avino, S. Pfeiffer, G. Rosaz, M. Taborelli, L. Vega-Cid, and W. Venturini-Delsolaro, Enhanced radiofrequency performance of niobium films on copper substrates deposited by high power impulse magnetron sputtering, Supercond. Sci. Technol. **35**, 054008 (2022).

[36] S. Keckert, W. Ackermann, H. De Gersem, X. Jiang, AÖ Sezgin, M. Vogel, M. Wenskat, R. Kleindienst, J. Knobloch, O. Kugeler, *et al.*, Mitigation of parasitic losses in the quadrupole resonator enabling direct measurements of low residual resistances of SRF samples, AIP Adv. **11**, 125326 (2021).

[37] Colt James, Mahadevan Krishnan, Brian Bures, Tsuyoshi Tajima, Leonardo Civale, Randy Edwards, Josh Spradlin, and Hitoshi Inoue, Superconducting Nb thin films on Cu for applications in SRF accelerators, IEEE Trans. Appl. Supercond. **23**, 3500205 (2012).

[38] Claire Z. Antoine, M. Aburas, A. Four, F. Weiss, Y. Iwashita, H. Hayano, S. Kato, Takayuki Kubo, and T. Saeki, Optimization of tailored multilayer superconductors

for RF application and protection against premature vortex penetration, Supercond. Sci. Technol. **32**, 085005 (2019).

[39] G. Lamura, M. Aurino, A. Andreone, and J.-C. Villégier, First critical field measurements of superconducting films by third harmonic analysis, J. Appl. Phys. **106**, 053903 (2009).

[40] C. Z. Antoine, S. Berry, S. Bouat, J. F. Jacquot, J. C. Villegier, G. Lamura, and A. Gurevich, Characterization of superconducting nanometric multilayer samples for superconducting rf applications: First evidence of magnetic screening effect, Phys. Rev. Spec. Top.-Accel. Beams **13**, 121001 (2010).

[41] C. Z. Antoine, S. Berry, M. Aurino, J.-F. Jacquot, J.-C. Villegier, G. Lamura, and A. Andreone, Characterization of field penetration in superconducting multilayers samples, IEEE Trans. Appl. Supercond. **21**, 2601 (2011).

[42] C. Z. Antoine, J.-C. Villegier, and G. Martinet, Study of nanometric superconducting multilayers for RF field screening applications, Appl. Phys. Lett. **102**, 102603 (2013).

[43] N. Katyan and C. Z. Antoine, Characterization of thin films using local magneometer, Tech. Rep., 2015, https://inspirehep.net/literature/1482097.

[44] Muhammad Aburas, C. Z. Antoine, and Aurelien Four, in *Proc. 18th Int. Conf. RF Superconductivity (SRF'17)* (2017), p. 830, https://accelconf.web.cern.ch/srf2017/doi/JACoW-SRF2017-THPB038.html.

[45] Hayato Ito, H. Hayano, T. Kubo, T. Saeki, Y. Iwashita, R. Katayama, H. Tongu, Kyoto ICR, R. Ito, T. Nagata, *et al.*, in *29th Linear Accelerator Conf.(LINAC'18), Beijing, China, 16–21 September 2018* (JACOW Publishing, Geneva, Switzerland, 2019), p. 484, https://accelconf.web.cern.ch/linac2018/doi/JACoW-LINAC2018-TUPO066.html.

[46] Hayato Ito, Hitoshi Hayano, Takayuki Kubo, and Takayuki Saeki, Vortex penetration field measurement system based on third-harmonic method for superconducting RF materials, Nucl. Instrum. Methods Phys. Res. Section A, **955**, 163284 (2020).

[47] Sheng-Chiang Lee, C. P. Vlahacos, B. J. Feenstra, Andrew Schwartz, D. E. Steinhauer, F. C. Wellstood, and Steven M. Anlage, Magnetic permeability imaging of metals with a scanning near-field microwave microscope, Appl. Phys. Lett. **77**, 4404 (2000).

[48] Sheng-Chiang Lee and Steven M. Anlage, Spatially-resolved nonlinearity measurements of $YBa_2Cu_3O_{7-\delta}$ bicrystal grain boundaries, Appl. Phys. Lett. **82**, 1893 (2003).

[49] Sheng-Chiang Lee, Mathew Sullivan, Gregory R. Ruchti, Steven M. Anlage, Benjamin S. Palmer, B. Maiorov, and E. Osquiguil, Doping-dependent nonlinear Meissner effect and spontaneous currents in high-T_c superconductors, Phys. Rev. B **71**, 014507 (2005).

[50] Sheng-Chiang Lee, Su-Young Lee, and Steven M. Anlage, Microwave nonlinearities of an isolated long $YB_{a2}Cu_3O_{7-\delta}$ bicrystal grain boundary, Phys. Rev. B **72**, 024527 (2005).

[51] Dragos I. Mircea, Hua Xu, and Steven M. Anlage, Phase-sensitive harmonic measurements of microwave nonlinearities in cuprate thin films, Phys. Rev. B **80**, 144505 (2009).

[52] Tamin Tai, X. X. Xi, C. G. Zhuang, Dragos I. Mircea, and Steven M. Anlage, Nonlinear near-field microwave

microscope for RF defect localization in superconductors, IEEE Trans. Appl. Supercond. **21,** 2615 (2011).

[53] Tamin Tai, Behnood G. Ghamsari, and Steven M. Anlage, Nanoscale electrodynamic response of Nb superconductors, IEEE Trans. Appl. Supercond. **23,** 7100104 (2012).

[54] Tamin Tai, B. G. Ghamsari, and Steven M. Anlage, Modeling the nanoscale linear response of superconducting thin films measured by a scanning probe microwave microscope, J. Appl. Phys. **115,** 203908 (2014).

[55] Tamin Tai, Behnood G. Ghamsari, Thomas R. Bieler, Teng Tan, X. X. Xi, and Steven M. Anlage, Near-field microwave magnetic nanoscopy of superconducting radio frequency cavity materials, Appl. Phys. Lett. **104,** 232603 (2014).

[56] Tamin Tai, Behnood G. Ghamsari, Tom Bieler, and Steven M. Anlage, Nanoscale nonlinear radio frequency properties of bulk Nb origins of extrinsic nonlinear effects, Phys. Rev. B **92,** 134513 (2015).

[57] Bakhrom Oripov, Thomas Bieler, Gianluigi Ciovati, Sergio Calatroni, Pashupati Dhakal, Tobias Junginger, Oleg B. Malyshev, Giovanni Terenziani, Anne-Marie Valente-Feliciano, Reza Valizadeh, *et al.*, High-frequency nonlinear response of superconducting cavity-grade Nb surfaces, Phys. Rev. Appl. **11,** 064030 (2019).

[58] Anne-Marie Valente-Feliciano, Superconducting RF materials other than bulk niobium: A review, Supercond. Sci. Technol. **29,** 113002 (2016).

[59] V. Arbet-Engels, Cristoforo Benvenuti, S. Calatroni, Pierre Darriulat, M. A. Peck, A.-M. Valente, and C. A. Van't Hof, Superconducting niobium cavities a case for the film technology, Nucl. Instrum. Methods Phys. Res. Section A, **463,** 1 (2001).

[60] Alban Sublet, Walter Venturini Delsolaro, Mathieu Therasse, Thibaut Richard, Guillaume Rosaz, Sarah Aull, Pei Zhang, Barbora Bártová, Sergio Calatroni, and Mauro Taborelli, in *Proceedings of the 17th International Conference on RF Superconductivity* (JACoW, Geneva, Switzerland, 2015), pp. 617–621, https://cds.cern.ch/record/2288263.

[61] W. M. Roach, D. B. Beringer, J. R. Skuza, W. A. Oliver, C. Clavero, C. E. Reece, and R. A. Lukaszew, Niobium thin film deposition studies on copper surfaces for superconducting radio frequency cavity applications, Phys. Rev. Spec. Top.-Accel. Beams **15,** 062002 (2012).

[62] Guillaume Rosaz, Aleksandra Bartkowska, Carlota P. A. Carlos, Thibaut Richard, and Mauro Taborelli, Niobium thin film thickness profile tailoring on complex shape substrates using unbalanced biased high power impulse magnetron sputtering, Surface Coat. Technol. **436,** 128306 (2022).

[63] M. Ghaemi, A. Lopez-Cazalilla, K. Sarakinos, G. J. Rosaz, C. P. A. Carlos, S. Leith, S. Calatroni, M. Himmerlich, and F. Djurabekova, Growth of Nb films on Cu for superconducting radio frequency cavities by direct current and high power impulse magnetron sputtering: A molecular dynamics and experimental study, Surf. Coat. Technol. **476,** 130199 (2024).

[64] S. Posen, M. Liepe, and D. L. Hall, Proof-of-principle demonstration of Nb$_3$Sn superconducting radiofrequency cavities for high Q applications, Appl. Phys. Lett. **106,** 082601 (2015).

[65] Sam Posen and Daniel Leslie Hall, Nb$_3$Sn superconducting radiofrequency cavities: Fabrication, results, properties, and prospects, Supercond. Sci. Technol. **30,** 033004 (2017).

[66] Y. Trenikhina, S. Posen, A. Romanenko, M. Sardela, J. M. Zuo, D. L. Hall, and M. Liepe, Performance-defining properties of Nb$_3$Sn coating in SRF cavities, Supercond. Sci. Technol. **31,** 015004 (2017).

[67] E. A. Ilyina, Guillaume Rosaz, Josep Busom Descarrega, Wilhelmus Vollenberg, A. J. G. Lunt, Floriane Leaux, Sergio Calatroni, W. Venturini-Delsolaro, and Mauro Taborelli, Development of sputtered Nb$_3$Sn films on copper substrates for superconducting radiofrequency applications, Supercond. Sci. Technol. **32,** 035002 (2019).

[68] Alexander Gurevich, Enhancement of rf breakdown field of superconductors by multilayer coating, Appl. Phys. Lett. **88,** 012511 (2006).

[69] Takayuki Kubo, Yoshihisa Iwashita, and Takayuki Saeki, Radio-frequency electromagnetic field and vortex penetration in multilayered superconductors, Appl. Phys. Lett. **104,** 032603 (2014).

[70] Takayuki Kubo, Multilayer coating for higher accelerating fields in superconducting radio-frequency cavities: A review of theoretical aspects, Supercond. Sci. Technol. **30,** 023001 (2016).

[71] S. Calatroni, 20 years of experience with the Nb/Cu technology for superconducting cavities and perspectives for future developments, Physica C **441,** 95 (2006).

[72] Cristoforo Benvenuti, N. Circelli, and M. Hauer, Niobium films for superconducting accelerating cavities, Appl. Phys. Lett. **45,** 583 (1984).

[73] Sarah Aull, Walter Venturini Delsolaro, Tobias Junginger, Anne-Marie Valente-Feliciano, Jens Knobloch, Alban Sublet, and Pei Zhang, On the understanding of Q-slope of niobium thin films (2015), https://inspirehep.net/literature/1482050.

[74] V. Palmieri and R. Vaglio, Thermal contact resistance at the Nb/Cu interface as a limiting factor for sputtered thin film RF superconducting cavities, Supercond. Sci. Technol. **29,** 015004 (2015).

[75] Nickolas Groll, Alexander Gurevich, and Irinel Chiorescu, Measurement of the nonlinear Meissner effect in superconducting Nb films using a resonant microwave cavity: A probe of unconventional pairing symmetries, Phys. Rev. B **81,** 020504 (2010).

[76] Junki Makita, C. Sundahl, Gianluigi Ciovati, C. B. Eom, and Alex Gurevich, Nonlinear Meissner effect in Nb$_3$Sn coplanar resonators, Phys. Rev. Res. **4,** 013156 (2022).

[77] Alexander Gurevich and Gianluigi Ciovati, Dynamics of vortex penetration, jumpwise instabilities, and nonlinear surface resistance of type-II superconductors in strong rf fields, Phys. Rev. B **77,** 104501 (2008).

[78] L. Vega Cid, G. Bellini, A. Bianchi, L. M. A. Ferreira, S. B. Leith, C. Pereira Carlos, G. J. Rosaz, and W. Venturini Delsolaro, in *Proc. 21th Int. Conf. RF Supercond. (SRF'23)*, International Conference on RF Superconductivity No. 21 (JACoW Publishing, Geneva, Switzerland, 2023), p. 621, https://accelconf.web.cern.ch/srf2023/doi/JACoW-SRF2023-WEIXA02.html.

[79] Bakhrom Oripov and Steven M. Anlage, Time-dependent Ginzburg-Landau treatment of rf magnetic vortices in

superconductors: Vortex semiloops in a spatially nonuniform magnetic field, Phys. Rev. E **101**, 033306 (2020).

[80] Alden R. Pack, Jared Carlson, Spencer Wadsworth, and Mark K. Transtrum, Vortex nucleation in superconductors within time-dependent Ginzburg-Landau theory in two and three dimensions: Role of surface defects and material inhomogeneities, Phys. Rev. B **101**, 144504 (2020).

[81] Yusuke Kato, Charging effect on the Hall conductivity of single vortex in type II superconductors, J. Phys. Soc. Jpn. **68**, 3798 (1999).

[82] Antonio Lara, Farkhad G. Aliev, Alejandro V. Silhanek, and Victor V. Moshchalkov, Microwave-stimulated superconductivity due to presence of vortices, Sci. Rep. **5**, 9187 (2015).

[83] O. V. Dobrovolskiy, C. González-Ruano, A. Lara, R. Sachser, V. M. Bevz, V. A. Shklovskij, A. I. Bezuglyj, R. V. Vovk, M. Huth, and F. G. Aliev, Moving flux quanta cool superconductors by a microwave breath, Commun. Phys. **3**, 64 (2020).

[84] Alexander D. Hernández and Daniel Domínguez, Dissipation spots generated by vortex nucleation points in mesoscopic superconductors driven by microwave magnetic fields, Phys. Rev. B **77**, 224505 (2008).

[85] See the Supplemental Material at http://link.aps.org/supplemental/10.1103/PhysRevApplied.22.054010 for the parameter setting of the animations of rf vortex semiloop nucleation.

[86] Michael Tinkham, *Introduction to Superconductivity* (Dover Publications, Mineola, NY, 2004).

[87] J. Halbritter, On the oxidation and on the superconductivity of niobium, Appl. Phys. A **43**, 1 (1987).

[88] Warren DeSorbo, Effect of dissolved gases on some superconducting properties of niobium, Phys. Rev. **132**, 107 (1963).

[89] C. C. Koch, J. O. Scarbrough, and D. M. Kroeger, Effects of interstitial oxygen on the superconductivity of niobium, Phys. Rev. B **9**, 888 (1974).

[90] Denise C. Ford, Lance D. Cooley, and David N. Seidman, First-principles calculations of niobium hydride formation in superconducting radio-frequency cavities, Supercond. Sci. Technol. **26**, 095002 (2013).

[91] S. Isagawa, Hydrogen absorption and its effect on low-temperature electric properties of niobium, J. Appl. Phys. **51**, 4460 (1980).

[92] Armen Gulian, *Shortcut to Superconductivity* (Springer Nature, Cham, Switzerland, 2020).

Correction: A minor error in wording in the second sentence of Appendix G was introduced during the production process and has been fixed.